A spatio-temporal hybrid approach for mathematical epidemiological metapopulation models: Combining stochastic ensemble simulations with moment-closure approximations

Julia Bicker [a,*], Kilian Volmer [b], Jan Hasenauer [b], Martin J. Kühn [a,b]

[a] *Institute of Software Technology, Department of High-Performance Computing, German Aerospace Center, Cologne, Germany*
[b] *Bonn Center for Mathematical Life Sciences and Life & Medical Sciences Institute, University of Bonn, Bonn, Germany*

Abstract

Mathematical models support the evaluation of interventions to mitigate disease spread and inform public health decision-making. However, capturing stochastic epidemic dynamics across connected populations can be computationally demanding. While moment equations offer an efficient alternative to stochastic ensemble simulations, their accuracy depends on the dynamical regime. Hybrid models are a promising tool for combining the efficiency of moment-closure approximations with the detail of stochastic ensemble simulations, thereby balancing the trade-off between accuracy and computational complexity. In this work, we present a spatio-temporal hybrid framework in which each region of a metapopulation model switches independently between representations, guided by ensemble-level statistics. We systematically assess the accuracy of the moment-closure approximation and evaluate how switching criteria, initial conditions, and model parameters affect hybrid accuracy and runtime. An application to seasonal influenza-like illness dynamics in Germany illustrates the framework's use for regional intervention scenarios, with runtime reductions of up to 95% relative to the stochastic benchmark.

Keywords: Multiscale modeling, hybrid modeling, Method of Moments, Markov models, infectious diseases, scientific computing, MEmilio framework

1. Introduction

Mathematical models have become the principal tool for predicting and assessing the dynamics of epidemic outbreaks [1]. Modeling approaches can be broadly categorized based on their resolution and dynamics. Population-based mean-field models describe the numbers or proportions of individuals in distinct epidemiological states [2, 3, 4]. Metapopulation models extend this representation by coupling subpopulations to account for spatial and demographic heterogeneity [5, 6, 7, 8, 9, 10, 11], whereas agent-based models explicitly represent individuals and their interactions [12, 13, 14, 15]. Dynamics can be formulated deterministically or stochastically. Deterministic population-based and metapopulation models, commonly formulated as ordinary differential equations (ODEs), are widely used because of their computational efficiency and established methods of analysis. While their simplest formulations assume homogeneous mixing, more complex formulations can account for heterogeneous contact patterns between population

*Corresponding author
Email addresses: julia.bicker@dlr.de (Julia Bicker), kilian.volmer@uni-bonn.de (Kilian Volmer), jan.hasenauer@uni-bonn.de (Jan Hasenauer), martin.kuehn@dlr.de (Martin J. Kühn)

groups [16, 17]. However, deterministic models neglect random fluctuations in infection and recovery events, which can strongly influence epidemic dynamics, especially when only a small number of individuals is infected. Stochastic formulations capture these fluctuations at both the individual and the population level, but often entail higher computational costs.

Continuous-time Markov chains (CTMCs) provide a flexible framework for stochastic epidemic modeling [18, 19, 20]. Agent-based models with Markovian transition rules can be formulated as CTMCs and, when transition rates depend only on population counts, recast as population-based or metapopulation CTMCs. Non-exponentially distributed dwell times, such as infectious periods, can also be represented or approximated by introducing auxiliary stages using the linear chain trick and its generalizations [21]. This retains the Markov property in the enlarged state space while allowing flexible dwell-time distributions within epidemiological compartments [22]. Individual trajectories can be generated using exact stochastic simulation algorithms, such as the Gillespie algorithm [23]. However, the computational cost grows at least linearly with the number of simulated events. Consequently, (repeated) simulations of large populations can become computationally demanding.

While individual CTMC trajectories are stochastic, the corresponding probability distribution is governed by the master equation (ME), an ODE system describing the probability of being in a specific state at a given time. As the number of possible configurations grows rapidly with population size and model complexity, solving the ME quickly becomes computationally intractable. Instead, the method of moments (MoM) can be used to derive ODEs for statistical properties of this distribution, such as means, variances, and covariances [24, 25, 26]. For nonlinear transition propensities, lower-order moment equations generally depend on higher-order moments, requiring moment-closure approximations to obtain a tractable system. Various closure schemes have been proposed, including truncation [27], distributional closures [18, 28, 29], derivative matching [30, 31], and conditional closures [32]. The resulting moment equations provide a computationally efficient approximation of the statistical properties of stochastic epidemic dynamics. However, their accuracy depends on the chosen closure scheme and the dynamical regime. Moreover, a finite set of low-order moments does not generally determine the full probability distribution or the statistics of individual trajectories, limiting the direct assessment of outcomes such as epidemic extinction.

The prior considerations highlight that each modeling approach has distinct advantages and inherent limitations, thus choosing an appropriate model depends on the specific epidemiological context, population structure, and desired level of detail, with implications for both accuracy and computational cost. Hybrid modeling approaches aim to balance these requirements by combining different model formulations across space and time. Spatial hybridization couples formulations assigned to different spatial regions. For example, Yoneyama et al. [33] developed a hybrid SARS model that couples local ODE-based models with a global infection layer to account for inter-region traffic. Related approaches were suggested by Kasereka et al. [34], who considered different reproduction numbers for a network of cities, and Bradhurst et al [35], who simulated disease spread on a graph of livestock herds. While these models combine aspects of ODE- and network- or agent-based modeling, they still use population-based modeling assumptions and are thus similar to (graph-based) metapopulation approaches [11]. Other spatial hybrid approaches combine agent-based and ODE-based models [36], PDE- and ODE-based models [37], agent-based and PDE-based models [38], or empirically derived contact networks for mass gathering events with stochastic metapopulation models [39].

Temporal hybridization instead switches between formulations as the epidemic evolves. Bobashev et al. [40] proposed switching between a stochastic agent-based and a deterministic ODE-based model according to a case number threshold. Based on the idea that stochastic agent-based models are more appropriate to simulate disease dynamics in low incidence regimes than population-based models, this approach retains

an individual-level stochastic description when case numbers are low and uses a computationally efficient deterministic description when case numbers are sufficiently large. Hunter et al. [41] investigated a related approach for disease spread at town and county levels.

Recently, we presented a general framework for spatial and temporal hybridization of agent- and metapopulation-based models [42], using model formulations originally introduced in [19]. In the spatial hybridization, an agent-based model describes disease spread in a focus region, while ODEs describe dynamics in connected regions. In the temporal hybridization, the system switches between stochastic agent-based and deterministic population-based descriptions during the simulation. The resulting hybrid models reproduced key features of the agent-based dynamics, including epidemic extinction, while reducing runtime and energy consumption by up to 98 %. These results illustrate the potential of hybrid modeling. However, determining how, where and when to switch between formulations remains a central methodological challenge. In particular, switching criteria must balance computational savings against the accuracy required to capture stochastic epidemic dynamics.

In this study, we combine the distinct spatial and temporal hybridization approaches introduced in [42] in a novel spatio-temporal hybrid model and apply this framework to a continuous-time Markov model and the corresponding system of mean and moment equations. We first analyze the runtime scaling of both the moment-closure approximation and the stochastic model with respect to the population size and the number of modeled regions, quantifying the computational advantage of the moment equations. Second, we systematically investigate the accuracy of the moment-closure approximation under varying initial conditions. This analysis enables the derivation of criteria that determine when the moment-closure approximation is sufficiently accurate and when the stochastic representation is required. We then apply four distinct conditions to spatio-temporal hybrid SIR- and SIRS-type metapopulation models and evaluate the switching behavior, the accuracy relative to a fully stochastic reference, and the strong scaling behavior. Finally, we use the spatio-temporal hybrid model to simulate the spread of influenza-like illness (ILI) in Germany from August 2016 to July 2021, assessing the impact of various non-pharmaceutical interventions (NPIs) as decreed for mitigating COVID-19 from March 2020 onward. The results demonstrate the hybrid model's ability to accurately capture local outbreaks as well as long-term epidemic dynamics, highlighting its potential for epidemic forecasting and scenario analysis.

2. Materials and Methods

2.1. Stochastic metapopulation model

In this manuscript, we consider stochastic metapopulation models of infectious disease dynamics formulated as continuous-time Markov chains. Given n_Z epidemiological states and n_R spatial regions, resulting in $n_C = n_Z \cdot n_R$ subpopulations (or compartments), the system state is given by the stacked vector

$$X(t) = \left(X^{(1)}(t)^\top, \ldots, X^{(n_R)}(t)^\top\right)^\top \in \mathbb{N}_0^{n_C},$$

where

$$X^{(k)} = \left(X_1^{(k)}, \ldots, X_{n_Z}^{(k)}\right)^\top$$

records the numbers of individuals in region $k \in \{1, \ldots, n_R\}$ and $X_z^{(k)}(t)$ denotes the number of individuals in region k having epidemiological state $z \in \{1, \ldots, n_Z\}$. For readability, we also use an equivalent flat indexing, $X(t) = (X_1(t), \ldots, X_{n_C}(t))^\top$, and an index mapping $\iota(z, k) = (k-1)n_Z + z$ with

$$X_{\iota(z,k)} = X_z^{(k)}.$$

The dynamics are specified by n_T transition types, describing changes in epidemiological state or movement between regions. Each transition type $r \in \{1, \dots, n_T\}$ has a (time-dependent) propensity $a_r : \mathbb{N}_0^{n_C} \times \mathbb{R}_{\geq 0} \to [0, \infty)$ and a change vector $\nu_r \in \mathbb{Z}^{n_C}$, whose i-th entry is the net change in subpopulation $i \in \{1, \dots, n_C\}$ for transition event r. When an event of type r occurs, the system state changes from x to $x + \nu_r$. The propensity $a_r(x, t)$ determines the rate of this event in state x at time t. While individual trajectories are stochastic, the probability distribution $P(x, t) := \mathbb{P}(X(t) = x)$ evolves according to the master equation,

$$\frac{\mathrm{d}}{\mathrm{d}t} P(x,t) = \sum_{r=1}^{n_T} \left[a_r(x - \nu_r, t) P(x - \nu_r, t) - a_r(x,t) P(x,t) \right], \tag{1}$$

which is a system of coupled ODEs. Terms associated with states outside the admissible state space are taken to be zero.

We sample individual trajectories using exact stochastic simulation algorithms [23, 43]. These algorithms generate successive transition events, with a computational cost that grows with the number of simulated events and the cost of selecting each event and updating the affected propensities. Consequently, simulations can become computationally demanding for large populations, fast transitions, or ensembles requiring many realizations. This motivates the use of moment equations which describe the evolution of moments of the CTMC's state distribution, together with moment-closure approximations, which yield a tractable system of equations.

2.2. Method of moments (MoM)

The MoM provides a system of ODEs describing the time evolution of mean, (co)variance, and higher-order (central) moments of the solution of the ME (Eq. 1). For CTMCs whose propensities are polynomial of degree at most two in the state variables, with possibly time-dependent coefficients, the derivation from [26] can be employed. Consequently, the mean $\mu = (\mu_1, \dots, \mu_{n_C})^\top$ is given by

$$\frac{d}{dt}\mu_c = \sum_{r=1}^{n_T} \nu_{r,c} \Big(a_r(\mu, t) + \frac{1}{2} \sum_{i,j=1}^{n_C} \frac{\partial^2 a_r(\mu, t)}{\partial X_i \partial X_j} \sigma_{i,j} \Big)$$

where $\nu_{r,c}$ denotes the c-th entry of ν_r. The mean number of individuals in subpopulation $c = 1, \dots, n_C$ depends on the (co)variances between subpopulations X_i and X_j, $\sigma_{i,j} = \mathbb{E}\left[(X_i - \mu_i)(X_j - \mu_j)\right]$, if there exist i and j such that $\frac{\partial^2 a_r(\mu,t)}{\partial X_i \partial X_j} \neq 0$. Hence, the means can depend on a set of central moments of order two. The governing equations for variances and covariances are given by

$$\begin{aligned}\frac{d}{dt}\sigma_{i,j} = \sum_{r=1}^{n_T} \Bigg[& \sum_{k=1}^{n_C} \frac{\partial a_r(\mu, t)}{\partial X_k} \Big(\nu_{r,i}\sigma_{j,k} + \nu_{r,j}\sigma_{i,k} \Big) + \nu_{r,i}\nu_{r,j} \Big(a_r(\mu, t) + \frac{1}{2} \sum_{k,l=1}^{n_C} \frac{\partial^2 a_r(\mu, t)}{\partial X_k \partial X_l} \sigma_{k,l} \Big) \\ & + \frac{1}{2} \sum_{k,l=1}^{n_C} \frac{\partial^2 a_r(\mu, t)}{\partial X_k \partial X_l} \Big(\nu_{r,i} \mathbb{E}[(X_j - \mu_j)(X_k - \mu_k)(X_l - \mu_l)] + \nu_{r,j} \mathbb{E}[(X_i - \mu_i)(X_k - \mu_k)(X_l - \mu_l)] \Big) \Bigg].\end{aligned}$$

Similar to the equations for mean and (co)variances, a general system of ODEs governing all central moments can be derived according to [26].

For systems involving quadratic or higher-order propensities, the moment equations of a given order may depend on moments of higher order, thus the resulting ODE system is not necessarily closed. Therefore, moment closure schemes that approximate higher-order moments in terms of lower-order ones are required to render the system solvable [44, 45]. While this introduces approximation error, the resulting

moment-closure approximations can be computed efficiently using standard ODE solvers, providing a computationally efficient alternative to estimating moments from stochastic simulation ensembles. In this study, the Boost implementation [46] of the adaptive Runge-Kutta-Cash-Karp54 method is used to solve ODE systems.

Although population size can influence the dynamics and thus the computational cost of solving the moment equations, the number of state variables remains unchanged. Consequently, the computational cost typically depends much weaker on population size than that of stochastic simulation algorithms, but scales with the number of ODEs governing the system which depends on the number of compartments.

2.3. Hybrid modeling approach

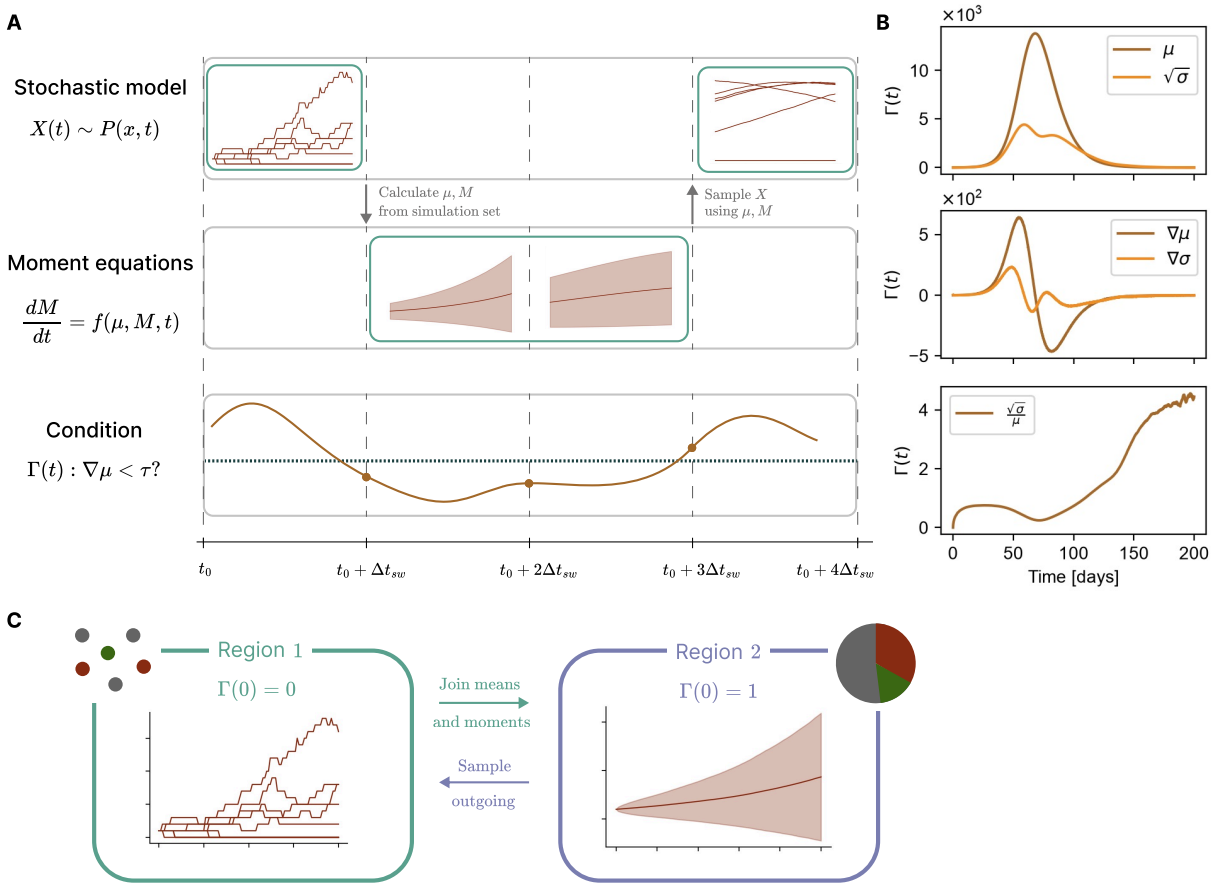


Figure 1: Overview of the hybrid modeling approaches. A: Temporal hybridization. The condition indicates which model is used and is evaluated at discrete time points in intervals Δt_{sw}. In the visualization, the moment-closure approximation is used if the mean gradient is below a threshold τ and Gillespie simulations are used if the mean gradient is above τ. **B:** Possible quantities used for a switching condition. Shown are the mean and standard deviation (top), their gradients (middle) and the relation of current mean and standard deviation (bottom) over time. **C:** Spatial hybridization. Region 1 uses stochastic simulations and region 2 uses the moment-closure approximation for simulation. Upon spatial transitions, the corresponding system states are adapted.

To combine the computational efficiency of the MoM with the accuracy of stochastic Gillespie simulations in regimes where the moment-closure approximation fails, we introduce a stochastic-deterministic

hybrid modeling approach. Based on [42], the hybrid model employs two types of hybridization: A temporal hybridization and a spatial hybridization.

For both approaches, we define two condition functions:

- $\Gamma^{(S\to D)} : \mathbb{N}_0^{n_C\times n_{sims}} \to \{0,1\}$, which maps the current system state of n_{sims} independent stochastic simulations to a binary value and returns 1 if the joint system state satisfies a predefined criterion for switching to the moment-closure approximation, and 0 otherwise.

- $\Gamma^{(D\to S)} : \mathbb{R}^{n_C+n_m} \to \{0,1\}$, which similarly maps the current MoM state, i.e., the solution of n_C mean and $n_m = \binom{m+n_C}{m} - n_C - 1$ central moment equations for moments up to order m, to a binary value indicating if a switch to the stochastic model is required.

Depending on the output of the condition functions, the system state is evolved either using stochastic simulations or the moment-closure approximation. This adaptive strategy ensures high fidelity in time frames or regions where an exact stochastic representation is necessary while maintaining efficiency in regimes where the moment-closure approximation is sufficient.

For a stochastic simulation $s \in \{1,\dots,n_{sims}\}$, let $X_{z,s}^{(k)}$ be the number of individuals in region k having epidemiological state z. The means of a stochastic ensemble of size n_{sims} are given by

$$\mu^S_{\iota(z,k)} = \frac{1}{n_{sims}} \sum_{s=1}^{n_{sims}} X_{z,s}^{(k)}, \tag{2}$$

and the (co)variances by

$$\sigma^S_{\iota(z,k),\iota(y,l)} = \frac{1}{n_{sims}-1} \sum_{s=1}^{n_{sims}} \left(X_{z,s}^{(k)} - \mu^S_{\iota(z,k)}\right)\left(X_{y,s}^{(l)} - \mu^S_{\iota(y,l)}\right). \tag{3}$$

We denote the means and (co)variances obtained from the moment-closure approximation by $\mu^D_{\iota(z,k)}$ and $\sigma^D_{\iota(z,k),\iota(y,l)}$, respectively.

In the temporal hybridization, the model switches dynamically between stochastic representation and moment-closure approximation during the simulation, hence $\Gamma^{(S\to D)}$ and $\Gamma^{(D\to S)}$ are evaluated in regular time intervals of size Δt_{sw} (Fig. 1A). This evaluation time step Δt_{sw} restricts the maximum integrator step size Δt_{max} used for solving the moment equations. If the switching condition is fulfilled, the whole system transitions from stochastic representation to moment-closure approximation, or vice versa. The condition is chosen in advance of the simulation and can depend on arbitrary statistics of the system state (Fig. 1B). Converting from stochastic model to moment equations is straightforward: The current mean and central moments are computed directly from the ensemble of stochastic simulations (see Eqs. 2 and 3) and used as initial conditions for the moment equations. In contrast, the conversion from moment equations to stochastic model requires reconstruction of the current state of the stochastic ensemble. This is achieved by sampling the current state for each of the n_{sims} simulations from an appropriate probability distribution in line with the statistics given by the moment equations. In this study, we use the normal distribution specified in Eq. 4 to sample values for the stochastic ensemble. Since our analysis focuses on ensemble-level statistics rather than individual simulation outcomes, we do not explicitly enforce simulation-level properties such as population conservation.

For the spatial hybridization, different regions are modeled using distinct representations, based on a unique assignment at the beginning of the simulation governed by the condition function $\Gamma^{(S\to D)}$ (Fig. 1C). If the moment-closure approximation is used in a region, means are set to initial compartment values, while

moments of higher order are initialized with zero. To account for spatial transitions occurring between regions modeled with different model types, inter-model exchange of individuals is performed in regular intervals Δt_{ex}. This discrete inter-model exchange represents an approximation, as movement of individuals is in general not restricted to the model exchange time points. The approximation error depends on the choice of Δt_{ex}. Similar to Δt_{sw} in the temporal hybridization, Δt_{ex} is an upper limit for the maximum integrator step size. For the exchange from a region using moment equations to a stochastic region, the incoming group of individuals is sampled similar to the deterministic-stochastic conversion in the temporal hybridization. Precisely, for every simulation $s = 1, \ldots, n_{sims}$, the number of (incoming) individuals in region k having epidemiological state z is drawn according to

$$\tilde{X}^{(k)}_{z,s} \sim \mathcal{N}(\mu^D_{\iota(z,k)}, \sigma^D_{\iota(z,k),\iota(z,k)}). \tag{4}$$

In the spatial hybridization, these statistics refer to the subpopulation entering region k from all regions modeled with moment equations during the last step of size Δt_{ex}. Since sampling from the normal distribution may yield non-integer or negative values, sampled values are adjusted via

$$X^{(k)}_{z,s} = \max\{0, \lfloor \tilde{X}^{(k)}_{z,s} + \xi_{\iota(z,k),s-1} \rceil\}, \tag{5}$$

where $\xi_{\iota(z,k),s-1}$ is a cutoff and rounding error correction term intended to keep mean and variance of the sampled values close to the statistics obtained from the moment equations. $\lfloor \cdot \rceil$ denotes rounding to the nearest integer.

When exchanging subpopulations from a stochastically modeled region to a region using moment equations, the ODE system state is updated by merging the mean and moments of the incoming stochastic subpopulation with the existing ones. For the mean, this update is done by employing linearity of expectation:

$$\mu^D_{\iota(z,k)} \leftarrow \mu^D_{\iota(z,k)} + \mu^S_{\iota(z,k)}$$

To maintain computational tractability, we do not consider covariance contributions from incoming stochastic populations, i.e., we neither update covariances upon exchange of subpopulations between models nor use them to update variances. Variances are updated using the general inequality

$$\left(\sqrt{\mathrm{Var}[X]} - \sqrt{\mathrm{Var}[Y]} \right)^2 \leq \mathrm{Var}[X + Y] \leq \left(\sqrt{\mathrm{Var}[X]} + \sqrt{\mathrm{Var}[Y]} \right)^2. \tag{6}$$

Employing Eq. 6, the updated variance in a region k modeled with moment equations is sampled uniformly from

$$\begin{aligned} \tilde{\sigma}^D_{\iota(z,k),\iota(z,k)} &\sim U\left[\left(\sqrt{\sigma^D_{\iota(z,k),\iota(z,k)}} - \sqrt{\sigma^S_{\iota(z,k),\iota(z,k)}} \right)^2, \left(\sqrt{\sigma^D_{\iota(z,k),\iota(z,k)}} + \sqrt{\sigma^S_{\iota(z,k),\iota(z,k)}} \right)^2 \right] \\ \sigma^D_{\iota(z,k),\iota(z,k)} &\leftarrow \tilde{\sigma}^D_{\iota(z,k),\iota(z,k)}. \end{aligned}$$

The approximation above does not explicitly verify positive semi-definiteness of the complete covariance matrix. However, enforcing this property when reconstructing (co)variances is non-trivial and lies beyond the scope of this manuscript.

The two introduced hybridization approaches are complementary rather than mutually exclusive and can therefore be combined in a spatio-temporal hybrid framework (Supplementary Algorithm 1). In that case, we choose $\Delta t_{sw} = \Delta t_{ex}$, ensuring that within-region model switching and the exchange of subpopulations between populations of different representations occur at identical time intervals.

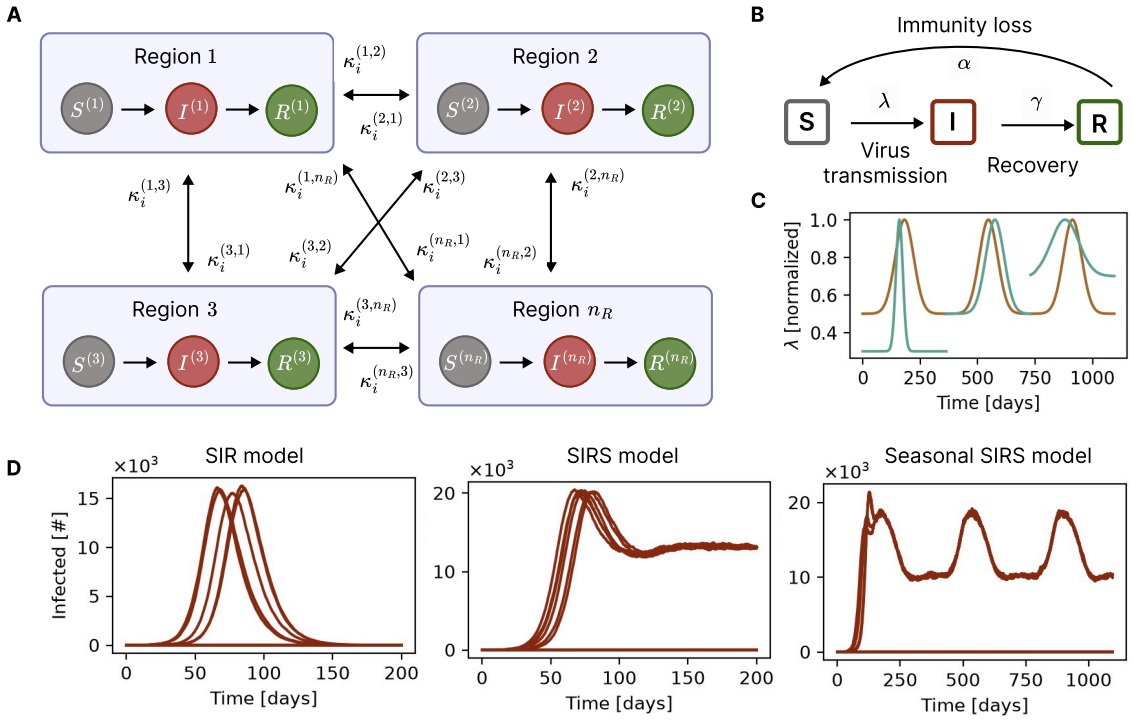


Figure 2: Overview of the stochastic model. **A:** Susceptible-Infected-Recovered (SIR) metapopulation model with spatial transition rates $\kappa_i^{(k,l)}$, $i \in \{S, I, R\}$. **B:** Flow chart of the SIRS type epidemiological model. **C:** Seasonal variation of the transmission rate λ given a normalized peak rate of $\lambda_0 = 1$. One setting with identical $\rho_s = 0.5, w_s = 40$ in every season and $t_s = 365 \cdot s + 182$, $s \in \{0, 1, 2\}$ (brown), and one setting with varying parameters per season ($(\rho_0, \rho_1, \rho_2) = (0.3, 0.5, 0.7)$, $(t_0, t_1, t_2) = (160, 365 + 210, 2 * 365 + 150)$, $(w_0, w_1, w_2) = (15, 40, 60)$) (teal). **D:** Exemplary trajectories for the SIR (left), the SIRS (middle) and the seasonal SIRS (right) model. Shown are 10 runs with identical parameters and initial conditions for each model.

2.4. Models for simulation study

In this study, we specialize the general CTMC formulation underlying the ME (Eq. 1) and consider three models of increasing complexity: (i) an SIR model describing infection and recovery, (ii) an SIRS model additionally accounting for waning immunity, and (iii) a seasonal SIRS model with time-dependent transmission rates. All three models describe a population distributed across n_R regions. Within each region, individuals are classified as *susceptible* (S), *infected* (I), or *recovered* (R), resulting in $n_C = 3n_R$ compartments (Fig. 2A). Therefore, the system state is $X(t) = \left(X^{(1)}(t)^\top, \ldots, X^{(n_R)}(t)^\top\right)^\top \in \mathbb{N}_0^{3n_R}$ with

$$X^{(k)}(t) = \left(X_S^{(k)}(t),\, X_I^{(k)}(t),\, X_R^{(k)}(t)\right)^\top. \tag{7}$$

We neglect births and deaths, so the total population size N remains constant over time, while regional population sizes can change through movement.

All three models include movement between distinct regions k and l, described by spatial transitions $z^{(k)} \to z^{(l)}$ with propensity $\kappa_z^{(k,l)} X_z^{(k)}(t)$. Here, $\kappa_z^{(k,l)}$ denotes the per-capita movement rate from region k to region l for individuals in epidemiological state $z \in \{S, I, R\}$. Movement preserves the individual's epidemiological state. The within-region transitions and their rates are specified below.

SIR model. The SIR model includes virus transmission and recovery (Fig. 2A). In region k, virus transmission from infected to susceptible individuals is described by the transition $S^{(k)} \to I^{(k)}$ with propensity $\lambda^{(k)} X_S^{(k)}(t) X_I^{(k)}(t)$, and recovery from infection by $I^{(k)} \to R^{(k)}$ with propensity $\gamma X_I^{(k)}(t)$. The transmission parameter $\lambda^{(k)}$ can vary between regions to account for differences in contact frequency and patterns, whereas the recovery rate γ is assumed to be identical across regions.

SIRS model. The SIRS model extends the SIR model by allowing immunity to wane after recovery (Fig. 2B), accounting for the possibility of reinfection in diseases such as influenza or COVID-19 [47, 48]. It includes the additional transition $R^{(k)} \to S^{(k)}$ with propensity $\alpha X_R^{(k)}(t)$, where the waning rate α is assumed to be identical across regions.

Seasonal SIRS model. The seasonal SIRS model retains the transitions of the SIRS model and introduces time-dependent transmission rates to account for seasonal variations. While these variations in transmission dynamics of infectious diseases are not entirely understood, potential drivers include temperature, humidity, and changes in indoor contact patterns [49]. Based on [50], we describe seasonality using a time-dependent transmission rate $\lambda : \mathbb{R}_{\geq 0} \to \mathbb{R}_{\geq 0}$ given by

$$\lambda(t) = \lambda_0 \left(\rho_s + (1 - \rho_s) \frac{g(t - t_s, w_s)}{g(0, w_s)} \zeta(t) \right), \tag{8}$$

where $\lambda_0 \in \mathbb{R}_{>0}$ is the peak transmission rate, $\rho_s \in [0, 1]$ the minimal transmission proportion in season $s \in \mathbb{N}_0$, $t_s \in \mathbb{R}_{\geq 0}$ the time point of peak transmission in season s and $g(t, w_s)$ is a Gaussian distribution with standard deviation $w_s \in \mathbb{R}_{>0}$ and mean zero. We assume a season length of one year, thus $s = \left\lfloor \frac{t}{365} \right\rfloor$. $\zeta : \mathbb{R}_{\geq 0} \to \mathbb{R}_{\geq 0}$ is a mixing function defined as

$$\zeta(t) = \begin{cases} \frac{1}{60}(t - \tau_s^- + 30), & \text{if } t < \tau_s^- + 30 \\ 1, & \text{if } \tau_s^- + 30 \leq t \leq \tau_s^+ - 30 \\ \frac{1}{60}(\tau_s^+ + 30 - t), & \text{if } t > \tau_s^+ - 30 \end{cases}$$

$\tau_s^- = 365s$ and $\tau_s^+ = \tau_s^- + 365$ denote the start and end time point of season s, respectively. Using identical seasonality settings across all seasons, i.e., $\rho_i = \rho_j$, $t_i = t_{i-1} + 365$, and $w_i = w_j$ for $i, j \in \mathbb{N}$ with given initial values ρ_0, t_0 and w_0, results in interchangeable temporal variation patterns of the transmission rate in each season. In contrast, varying the parameters between seasons generates season-specific transmission dynamics and leads to greater heterogeneity in the transmission rate across seasons (Fig. 2C).

Disease dynamics differ substantially among the SIR, the SIRS and the seasonal SIRS models. Although all three models capture virus extinction for an appropriate parameter choice in a single region, their behavior diverges when sustained transmission and outbreak events occur (Fig. 2D). Overall, we observed that the SIR model simulations produce, at maximum, one single epidemic wave after which infection dies out due to depletion of susceptible individuals. In contrast, given a sufficiently high transmission rate and fraction of initial susceptibles, in outbreak simulations the SIRS model initially exhibits an infection wave and subsequently converges to an equilibrium state, characterized by a persistent, non-negligible infection prevalence (Fig. 2D). The seasonal SIRS model, however, may produce recurrent epidemic waves in a single region which are driven by the temporal variations in the transmission rate.

Since the virus transmission transition $S^{(k)} \to I^{(k)}$ has a quadratic propensity, the moment equations for central moments of order two contain third-order central moments. To facilitate the numerical simulation, we therefore apply a truncation closure with $m = 2$, i.e.,

$$\mathbb{E}\left[(X_S^{(1)} - \mu_{\iota(S,1)})^{i_S^{(1)}} \dots (X_R^{(n_R)} - \mu_{\iota(R,n_R)})^{i_R^{(n_R)}} \right] = 0, \quad \forall (i_S^{(1)}, \dots, i_R^{(n_R)}) : i_S^{(1)} + \dots + i_R^{(n_R)} = 3.$$

Various alternatives to truncation closure exist, including closures based on distributional assumptions, however their accuracy depends on the model and parameter values (Supplementary Fig. C.10). The moment equations for the SIRS-type metapopulation model are provided in Supplementary Section Appendix A. The equations for the seasonal SIRS-type model follow by using the time-dependent transmission rate $\lambda(t)$ from Eq. 8 and those for the SIR-type model by setting the waning rate $\alpha = 0$.

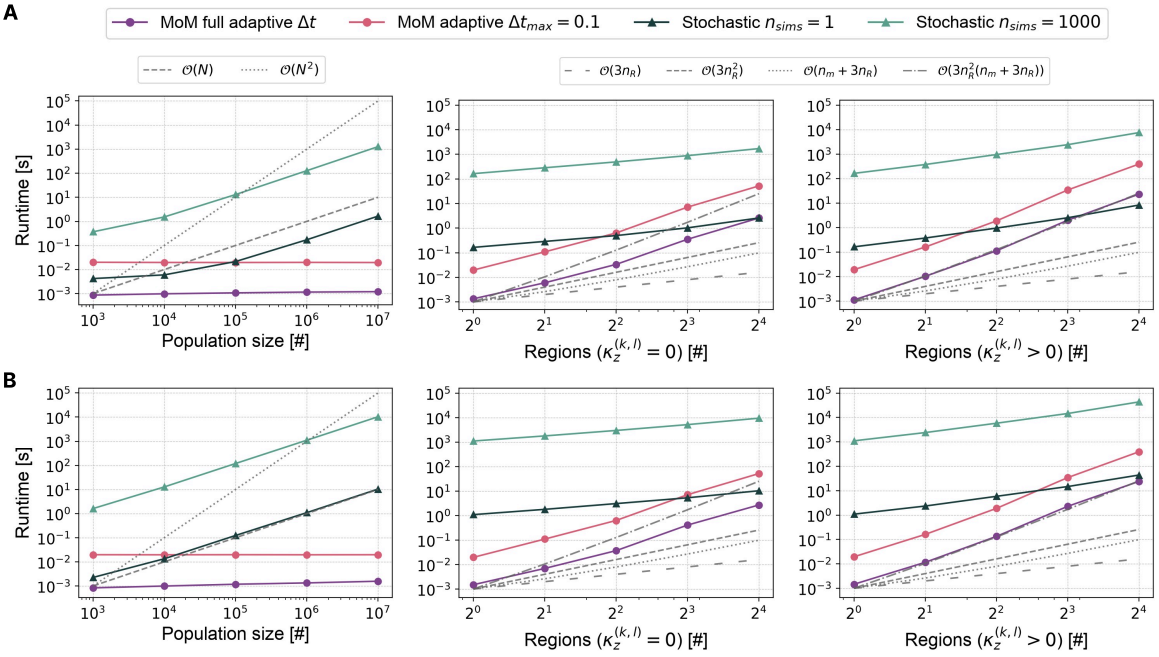


Figure 3: Scaling behavior of the stochastic model and the moment-closure approximation for varying population sizes (left) and a varying number of regions without (middle) and with (right) spatial transitions between regions. Shown are the results for sequential simulation on one core. For the stochastic model a set of 1 and 1000 simulations is shown. For the moment-closure approximation, we compare two settings: A fully adaptive integrator step size and an adaptive integrator step size constrained by a maximum step size of 0.1. Shown are the results for the **A:** SIR and the **B:** SIRS model.

3. Results

3.1. Runtime analysis of stochastic model and moment-closure approximation

To assess the challenge of using metapopulation models based on CTMCs for large-scale simulations, we compared the runtime scaling of stochastic ensembles and moment-closure approximations with respect to the population size and the number of regions. Therefore, we considered three settings for the SIR and SIRS-type models: (i) A single region with a total population size ranging from 10^3 to 10^7 individuals and an initial reproduction number of 2.5; (ii) a growing number of 1 to 16 regions with a total population size of 10^6, equally distributed across regions. The transmission rates were set such that the initial reproduction number in each region was 2.5 and no spatial transitions were considered i.e. $\kappa_z^{(k,l)} = 0, \forall\, k, l = 1, \ldots, n_R$, $z \in \{S, I, R\}$; (iii) the same setting as in (ii) with inter-regional mobility incorporated by using spatial transition rates $\kappa_z^{(k,l)} = 10^{-4}$ for $k \neq l$.

The parameters and initial conditions for all settings of the runtime analysis can be found in Supplementary Table D.1. We simulated the scenarios using the exact stochastic simulation algorithm (SSA) [43]

as well as the MoM with truncation closure. For the SSA, we compared the total runtime of 1 and 1,000 simulations. For the MoM, we used an unbound maximum integrator step size Δt_{max} as well as $\Delta t_{max} = 0.1$.

Our analysis for both models reveals that, on the one hand, the computational effort of the stochastic simulation increases with the number of modeled regions (Fig. 3, middle and right, settings (ii) and (iii)), as every region introduces additional transitions whose propensities have to be computed and updated. On the other hand, since propensities depend on compartment sizes, computational cost of the stochastic simulation also scales with the total population size (Fig. 3, left, setting (i)).

As the number of means and (central) moments depends on the number of modeled compartments, the computational cost of the MoM increases with the number of regions. Further, the evaluation of a given moment equation involves terms for spatial transitions (see Supplementary Eq. A.1). Consequently, the MoM exhibits lower runtimes for spatially independent regions compared to a fully connected region network (Fig. 3, middle and right, settings (ii) and (iii)). Additionally, the MoM runtime is influenced by the integrator step size. Allowing a fully adaptive step size reduces the MoM's runtime by approximately one order of magnitude compared to a constrained adaptive solver with a maximum step size of $\Delta t_{max} = 0.1$ (Fig. 3). This trade-off has to be considered when selecting Δt_{ex}, which is an upper bound for the maximum integrator step size in the hybrid model. Choosing the step size Δt_{ex} too small reduces the computational advantage of the hybrid model compared to the fully stochastic model. Conversely, a too large value of Δt_{ex} increases the approximation error due to a delayed incorporation of incoming subpopulations, leading to temporal inaccuracies.

For a single region with a modeled population of 10 million individuals, the MoM with a maximum step size of $\Delta t_{max} = 0.1$ is 82-times faster than a single run of the stochastic SIR-type model (setting (i)). When simulating an ensemble of 1,000 independent stochastic simulations sequentially, a speedup of five orders of magnitude is achieved (Fig. 3A, left). However, for a system with 16 regions and a total population size of 1 million – resulting in an ODE system of 1,224 coupled equations for the means and central moments of order two – the MoM with $\Delta t_{max} = 0.1$ and spatial transitions between regions (setting (iii)) is about 1.5 orders of magnitude slower than a single stochastic run (Fig. 3A, right). Nevertheless, for 1,000 stochastic runs executed sequentially, the MoM reaches a speedup of 33 and 19 under the same step size constraint without (Fig. 3A, middle, setting (ii)) and with (Fig. 3A, right, setting (iii)) spatial transitions between regions, respectively. Due to the increased number of transmission and waning immunity transitions, the runtime advantage of the MoM over the stochastic model is even bigger for the SIRS-type model (Fig. 3B). In that case, the MoM with bounded step size $\Delta t_{max} = 0.1$ is about 99 % faster than 1,000 simulations of the stochastic model for 16 regions and a total population of 1 million (settings (ii) and (iii)), and even 5.5 orders of magnitude for one region and a population of 10 million (setting (i)).

In summary, the analysis showed that for large population sizes and a small number of regions, the MoM is substantially faster than one individual CTMC simulation. However, when the number of regions is large, the MoM becomes slower than a single CTMC simulation due to the growing size of the ODE system as well as the increased number of spatial transition rates influencing each region. Nevertheless, since the MoM system needs to be solved only once, whereas reliable statistics from the CTMC usually require an ensemble of stochastic simulations, this additional cost is negligible as soon as various stochastic trajectories are needed.

3.2. Approximation performance of the MoM

To identify the configurations under which the MoM provides a good approximation to the underlying stochastic metapopulation model, we conducted a systematic parameter study for the SIR and the SIRS model, respectively (Figs. 4 and C.11A). For each configuration, we compared the mean and variance of

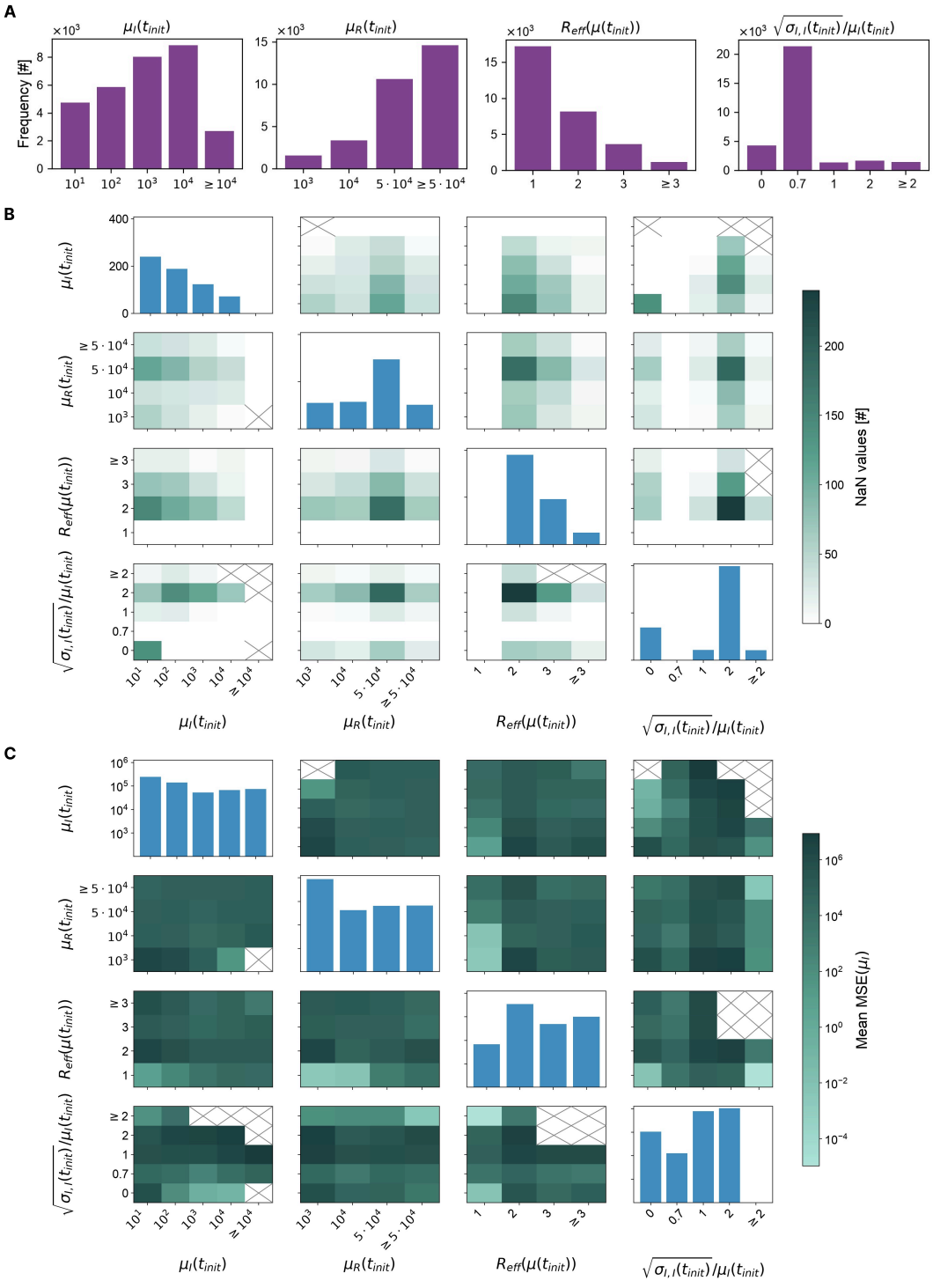


Figure 4: Performance analysis of the MoM for the SIR model. For the analysis, 50,000 stochastic runs were compared to the solution of the moment equations using truncation closure for each parameter set. **A:** Distribution of initial conditions. **B:** Distribution of NaN value counts. **C:** Mean MSE of the simulated mean number of infected μ_I.

50,000 independent stochastic simulations to the corresponding output of the moment-closure approximation. We considered four quantities: the mean number of infected μ_I and recovered μ_R, the standard deviation of the infected compartment $\sqrt{\sigma_{I,I}}$ and the reproduction number of the deterministic ODE-based compartmental model $R_{\mathit{eff}}(\mu) = \frac{\lambda}{\gamma} \cdot \mu_S$. The moment-closure approximation fails, i.e. the solver returns NaN values, in scenarios with initial values of $\mu_I < 10$ in combination with an initial standard deviation $\sqrt{\sigma_{I,I}}$ of zero or exceeding $0.7\mu_I$ (Figs. 4 and C.11B). However, for configurations with an initial reproduction number of the mean $R_{\mathit{eff}}(\mu(t_{init}))$ below one, the ODE system yields real-valued solutions for nearly all initial conditions. Additionally, the approximation error is minimal in this regime, as well as for initial conditions where $\frac{\sqrt{\sigma_{I,I}}}{\mu_I} < 0.7$, indicating that the relative variability of the infected population is low (Figs. 4, C.11 and C.12C). In contrast, the initial mean number of recovered does not exhibit a clear correlation with the accuracy of the moment-closure approximation.

From this parameter study, we derived the condition functions $\Gamma^{(S\to D)}$ and $\Gamma^{(D\to S)}$ described in Section 2.3 for the hybrid model. As the initial mean number of recovered does not show a clear influence on the accuracy of the moment-closure approximation, we based our conditions on the quantities μ_I, $\frac{\sqrt{\sigma_{I,I}}}{\mu_I}$ and $R_{\mathit{eff}}(\mu)$. For each of these, we defined separate conditions with corresponding thresholds or regimes where the moment-closure approximation performed well in our parameter study. We further introduced a fourth, combined condition that integrates all individual criteria. In addition to the quantity-dependent regimes, all condition functions use the moment-closure approximation, if the mean number of infectious individuals in a region falls below 1, indicating a regime where infections are unlikely in the most stochastic simulations and the moment-closure approximation is considered accurate. With $\mathbf{X} \in \mathbb{N}_0^{n_C \times n_{sims}}$ the matrix containing the system state of n_{sims} stochastic simulations, μ^D, Σ^D the vectors containing the means and central moments of order two of the moment-closure approximation and $R_{eff}^{(k)}(\mu) = \frac{\lambda^{(k)}}{\gamma}\mu_{\iota(S,k)}$, the four pairs of condition functions are defined as follows:

- An absolute threshold of $\tau_{\mu_{\iota(I,k)}} = 10$ for the mean number of infected:

$$\Gamma^{(S\to D)}(\mathbf{X}) = \begin{cases} 1, & \text{if } \mu^S_{\iota(I,k)} > 10 \vee \mu^S_{\iota(I,k)} < 1 \\ 0, & \text{otherwise} \end{cases}$$

$$\Gamma^{(D\to S)}([\mu^D, \Sigma^D]^\top) = \begin{cases} 1, & \text{if } \mu^D_{\iota(I,k)} < 10 \wedge \mu^D_{\iota(I,k)} \geq 1 \\ 0, & \text{otherwise} \end{cases}$$

- A threshold of 1 for the reproduction number of the mean $R_{eff}^{(k)}(\mu)$:

$$\Gamma^{(S\to D)}(\mathbf{X}) = \begin{cases} 1, & \text{if } R_{eff}^{(k)}(\mu^S) < 1 \vee \mu^S_{\iota(I,k)} < 1 \\ 0, & \text{otherwise} \end{cases}$$

$$\Gamma^{(D\to S)}([\mu^D, \Sigma^D]^\top) = \begin{cases} 1, & \text{if } R_{eff}^{(k)}(\mu^D) > 1 \wedge \mu^D_{\iota(I,k)} \geq 1 \\ 0, & \text{otherwise} \end{cases}$$

- An interval of $(0, 0.7)$ for the relation $\frac{\sqrt{\sigma_{\iota(I,k),\iota(I,k)}}}{\mu_{\iota(I,k)}}$ of standard deviation and mean of the infected com-

partment:

$$\Gamma^{(S\to D)}(\mathbf{X}) = \begin{cases} 1, & \text{if } \mu^S_{\iota(I,k)} \neq 0 \wedge \frac{\sqrt{\sigma^S_{\iota(I,k),\iota(I,k)}}}{\mu^S_{\iota(I,k)}} \in (0, 0.7) \\ 0, & \text{otherwise} \end{cases}$$

$$\Gamma^{(D\to S)}([\mu^D, \Sigma^D]^\top) = \begin{cases} 1, & \text{if } \mu^D_{\iota(I,k)} \neq 0 \wedge \left(\frac{\sqrt{\sigma^D_{\iota(I,k),\iota(I,k)}}}{\mu^D_{\iota(I,k)}} \leq 0 \vee \frac{\sqrt{\sigma^D_{\iota(I,k),\iota(I,k)}}}{\mu^D_{\iota(I,k)}} > 0.7 \right) \\ 0, & \text{otherwise} \end{cases}$$

- A combined condition integrating all previous ones:

$$\Gamma^{(S\to D)}(\mathbf{X}) = \begin{cases} 1, & \text{if } \mu^S_{\iota(I,k)} < 1 \vee R^{(k)}_{eff}\left(\mu^S\right) < 1 \vee \left(\frac{\sqrt{\sigma^S_{\iota(I,k),\iota(I,k)}}}{\mu^S_{\iota(I,k)}} \in (0, 0.7) \wedge \mu^S_{\iota(I,k)} > 10 \right) \\ 0, & \text{otherwise} \end{cases}$$

$$\Gamma^{(D\to S)}([\mu^D, \Sigma^D]^\top) = \begin{cases} 1, & \text{if } \mu^D_{\iota(I,k)} \geq 1 \wedge R^{(k)}_{eff}\left(\mu^D\right) > 1 \wedge \left(\frac{\sqrt{\sigma^D_{\iota(I,k),\iota(I,k)}}}{\mu^D_{\iota(I,k)}} > 0.7 \vee \mu^D_{\iota(I,k)} < 10 \right) \\ 0, & \text{otherwise} \end{cases}$$

In summary, the parameter study identifies regimes in which the moment-closure approximation accurately reproduces stochastic ensemble statistics, particularly when the reproduction number is below one or relative infection variability is low. These findings motivate four condition functions based on mean infection levels, relative variability, and the reproduction number, which we evaluate in the hybrid model in the following section.

3.3. Approximation and runtime performance of the hybrid model

To assess the potential of the hybrid modeling approach introduced in Section 2.3, we applied the spatio-temporal hybrid metapopulation model with the afore described conditions to both the SIR and SIRS model in a four-region setting with varying initial conditions in each region (Figs. 6 and C.13). We chose $\Delta t_{sw} = \Delta t_{ex} = 1$, hence we evaluated the condition functions and exchanged individuals between models once per day. Applying the error correction Eq. 5 significantly reduces deviation from target statistics compared to sampling without error correction (Fig. 5). As in the spatio-temporal hybrid model some regions can be modeled stochastically while others are modeled with the MoM, the system states of both models were synchronized at the desired output time steps, so that the overall output time series is obtained by simply summing their individual time series. We therefore saved the system states of both the stochastic model and the moment-closure approximation in regular intervals of 0.1 days. Due to the heterogeneous initial infection levels, the temporal evolution of the mean, the reproduction number, and the relative standard deviation varies across regions. This leads to region-dependent hybrid switching time points (Figs. 6 and C.13A). Although region 1 starts without initially infected, an outbreak occurs due to spatial transitions of infected individuals from neighboring regions. Nevertheless, the outbreak timing and magnitude differ between regions (Figs. 6 and C.13C), highlighting the need for spatial resolution when predicting realistic epidemic dynamics.

In regions 1 and 2, the moment-closure approximation and the hybrid model using the mean threshold condition $\tau_{\mu_{\iota(I,k)}} = 10$ fail to capture the stochastic model's reference dynamics (Figs. 6 and C.13C). In

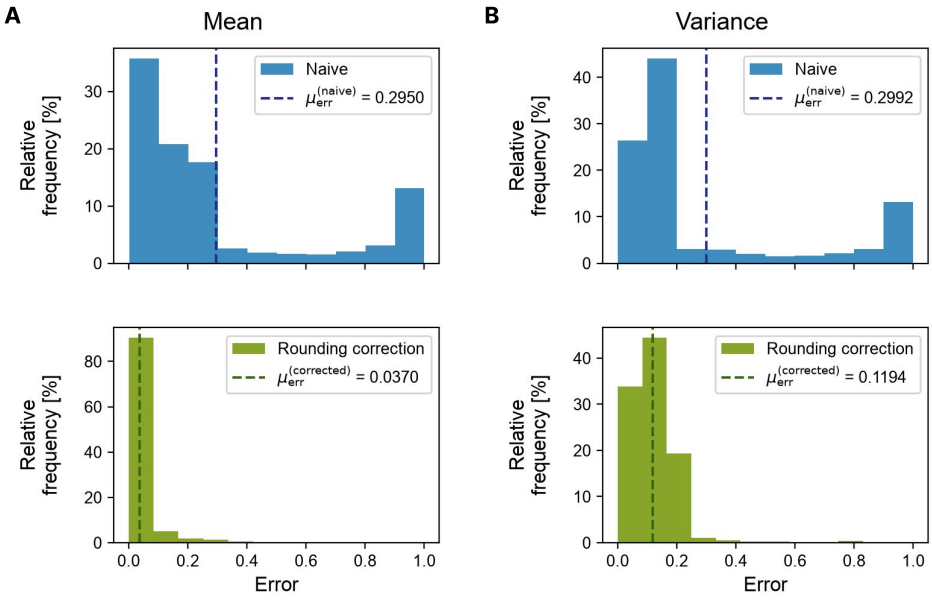


Figure 5: Sampling error comparison with (green) and without (blue) cutoff and rounding error correction. Shown are the distributions of the relative error of **A:** mean and **B:** variance.

contrast, the hybrid models using the standard deviation relation condition, the reproduction number condition and the combined condition are able to reproduce reference mean and variance. However, all hybrid models exhibit larger deviations from the stochastic model's mean in regions 1 and 2, where initial numbers of infected are small and stochastic fluctuations are more pronounced. The approximation of the standard deviation is less accurate than for the mean. Nevertheless, the hybrid model with the three aforementioned conditions is able to capture the overall temporal dynamics of it, including rise and decrease of the system's stochasticity. The hybrid model with the reproduction number condition performs best in terms of accuracy across all regions (Figs. 6 and C.13B), as it switches to the ODE-based formulation later in time than the other hybrid models. This in turn results in reduced runtime acceleration, however still achieving a speedup of ≈ 40 % on a single core (Figs. 6 and C.13D).

Using OpenMP for shared-memory parallelization, we investigated the strong scaling behavior of all implementations. While for the stochastic model only straightforward parallelization across individual simulations was applied, the hybrid model and moment-closure approximation also employ intra-model parallelization. We observe almost ideal strong scaling for the stochastic model on up to 128 cores. In contrast, both the moment-closure approximation and the hybrid models saturate at 32 cores the latest. This saturation is not further investigated but may arise from a combination of factors such as insufficient workload per thread at higher core counts or a transition from compute-bound to memory-bound behavior. The hybrid model using the standard deviation relation condition is $4-5$ times faster for the SIR model (Fig. 6D) and even $15-18$ times for the SIRS model (Fig. C.13D) on up to 32 cores. Beyond the saturation point, runtimes of moment-closure approximations and hybrid models increase due to parallelization overhead. The fastest setup, which is the hybrid model using the combined condition on 32 cores, reduces the runtime of the stochastic model on 128 cores by 30 and 80 %, respectively, while consuming only 25 % of the computational resources.

In a complementary scenario with identical numbers of initially infected across regions and varying

region-dependent transmission rates, the hybrid model using the reproduction number condition again outperforms the other hybrid models and the moment-closure approximation in terms of accuracy, however achieving less runtime reduction (Figs. C.14 and C.15).

The results presented above emphasize that the choice of appropriate condition functions critically influences both the accuracy and computational performance of the hybrid model.

3.4. Modeling the collective dynamics of influenza-like illnesses in Germany

To demonstrate the applicability of the hybrid modeling approach for epidemic spread, we used it to study and simulate the dynamics of the collection of ILI in Germany from 1st August 2016 until 27th July 2021. In a first step, we considered a global model for Germany with only one region and used the combined condition described in the previous section as condition function; with a mean infected threshold of 100 per 100,000 inhabitants, a standard deviation of $0.3\mu_I$ in the infected compartment and a reproduction number threshold of 1. Due to computational constraints, we modeled a population of size 835,771, representing one hundredth of Germany's total population. We assumed an average time from infection until recovery of 7 days; based on estimates for ILI symptom and shedding duration [51, 52], yielding a recovery rate $\gamma = \frac{1}{7}$. We used the size of the infected compartment (prevalence) as an approximation for the reported incidence. Initial conditions for the mean number of infected $\mu_I(t_0)$ and recovered $\mu_R(t_0)$ as well as the immunity loss rate and the transmission rate function parameters were calibrated against reported estimates for 7-day ILI incidence [53] from 1st August 2016 to 9th March 2020 (Fig. C.16). Calibration was performed using approximate Bayesian computation with the sequential Monte Carlo algorithm implemented in pyABC [54]. Priors for the peak transmission rate λ_0 were scaled with the modeled population size. The final parameters can be found in Table D.2.

As reaction to the first confirmed case of SARS-CoV-2 in Germany on 25th February 2020, a series of NPIs were implemented starting from 16th March 2020 onward [55], which also significantly altered transmission dynamics of ILI. To assess the impact of these interventions, we conducted a simulation study with the temporal-hybrid model and considered three scenarios:

- Baseline scenario (Base): Transmission dynamics continue unchanged from 9th March 2020 using season-specific parameters for the 2020/2021 ILI season (season 5) set as the mean values across prior seasons.

- Global NPIs scenario: Multiplicative damping factors $d^{(1)}, \ldots, d^{(6)} \in \mathbb{R}$ are applied to the transmission rate at six time points derived from [55]: $t_{d^{(1)}} = 1323$ (16th March 2020), $t_{d^{(2)}} = 1353$ (15th April 2020), $t_{d^{(3)}} = 1554$ (2nd November 2020), $t_{d^{(4)}} = 1577$ (25th November 2020), $t_{d^{(5)}} = 1680$ (8th March 2021) and $t_{d^{(6)}} = 1736$ (3rd May 2021). In this scenario $d^{(6)} = 1$, indicating that the previous change applied at 8th March 2021 remains in effect, implying partial persistence of NPIs and sustained suppression of transmission.

- Global NPIs total lifting scenario: Multiplicative damping factors are applied as in the Global NPIs scenario, but all interventions are fully lifted on 3rd May 2021, and the peak transmission rate is set to the value from before 16th March 2020.

The reported incidence shows a significant reduction from 9th March 2020 onward compared to previous seasons (Fig. 7A). The baseline scenario fails to reproduce this reduction in incidence levels, instead predicting an epidemic wave similar to the previous seasons. In contrast, the global intervention setting including both scenarios (with and without lifting in May 2021) captures the observed decline and produces only a minor wave in November 2020. While the continued intervention scenario also aligns with the data

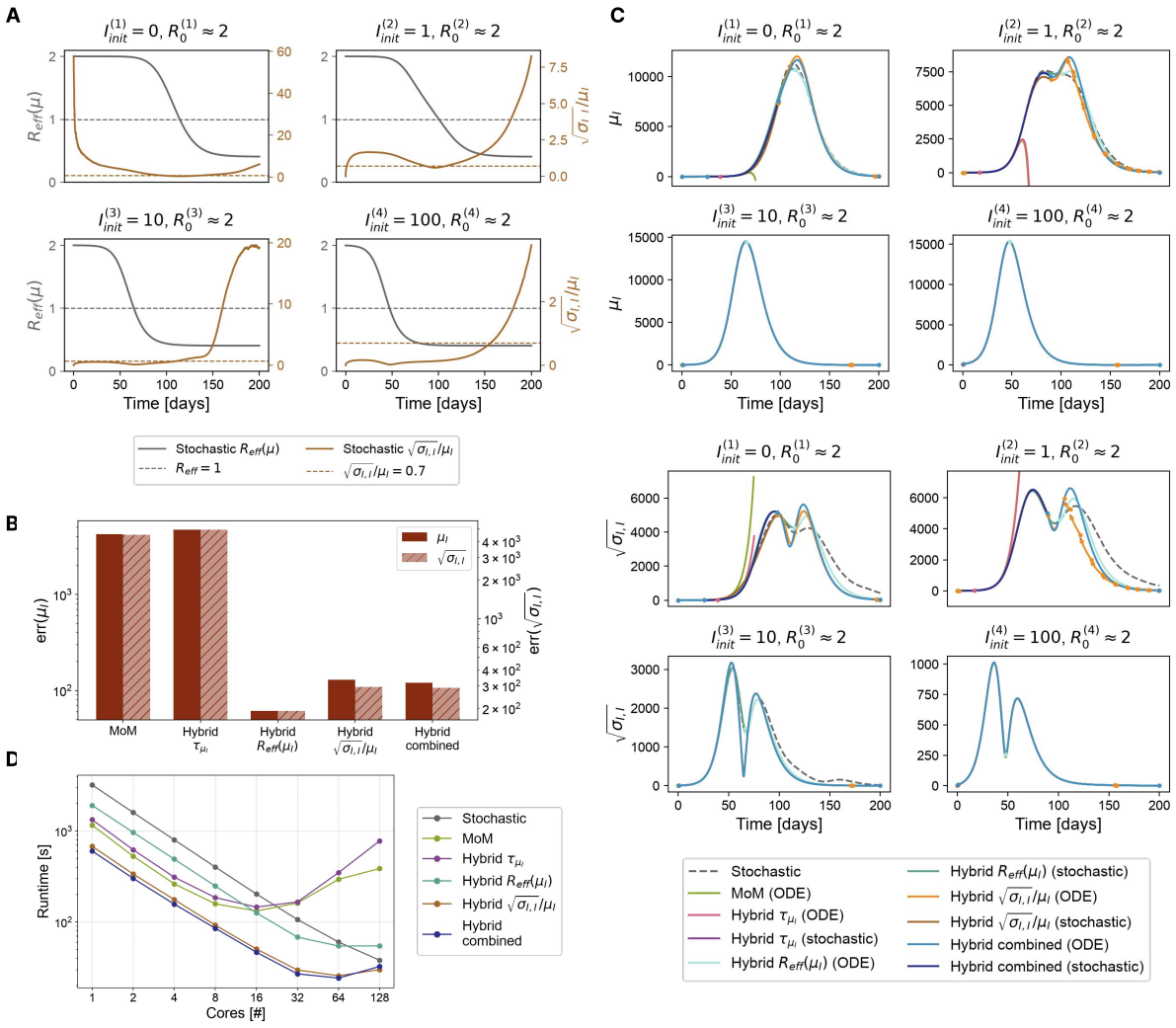


Figure 6: Results of different condition functions for the SIR-type model with four regions, an initial reproduction number $R_0^{(k)}, k \in \{1,2,3,4\}$, of approximately two, and a varying number of initially infected per region. For the stochastic model (and the stochastic parts of the hybrid models) $n_{sims} = 10{,}000$ simulations are considered. **A:** Temporal evolution of the effective reproduction number of the mean (grey) and the relative standard deviation of the infected compartment (brown) for each region in the stochastic model. The horizontal dashed lines indicate the threshold values used for the corresponding conditions. **B:** Mean absolute error in mean and standard deviation of the moment-closure approximation and the hybrid model with four different conditions. **C:** Evolution of mean (top) and standard deviation (bottom) in every region for the stochastic model, the moment-closure approximation and the hybrid model with four different conditions. For the hybrid model the stochastic parts are displayed in a dark and the moment-closure approximation parts in a light color shade. The dot markers indicate switching time point in the hybrid models. **D:** Strong scaling of the stochastic model (Stochastic), the moment-closure approximation (MoM), and the hybrid models using the absolute threshold condition (τ_{μ_I}), the reproduction number condition ($R_{eff}(\mu_I)$), the standard deviation relation condition ($\frac{\sqrt{\sigma_{I,I}}}{\mu_I}$) and the combined condition.

after May 2021, the total lifting scenario predicts a substantial increase in infections in May-July 2021, which is inconsistent with the observed data.

In the baseline scenario only the moment-closure approximation is used, while the other two scenarios

switch to the stochastic model for about 5 % of simulated time steps. Consequently, this leads to a runtime increase of approximately 30 % compared to the baseline scenario (Fig. 7B). However, the two intervention scenarios are still 95 % faster than simulating the baseline scenario with the stochastic model, which reflects the ability of the hybrid model to use the stochastic formulation only in critical regimes, while maintaining computational feasibility.

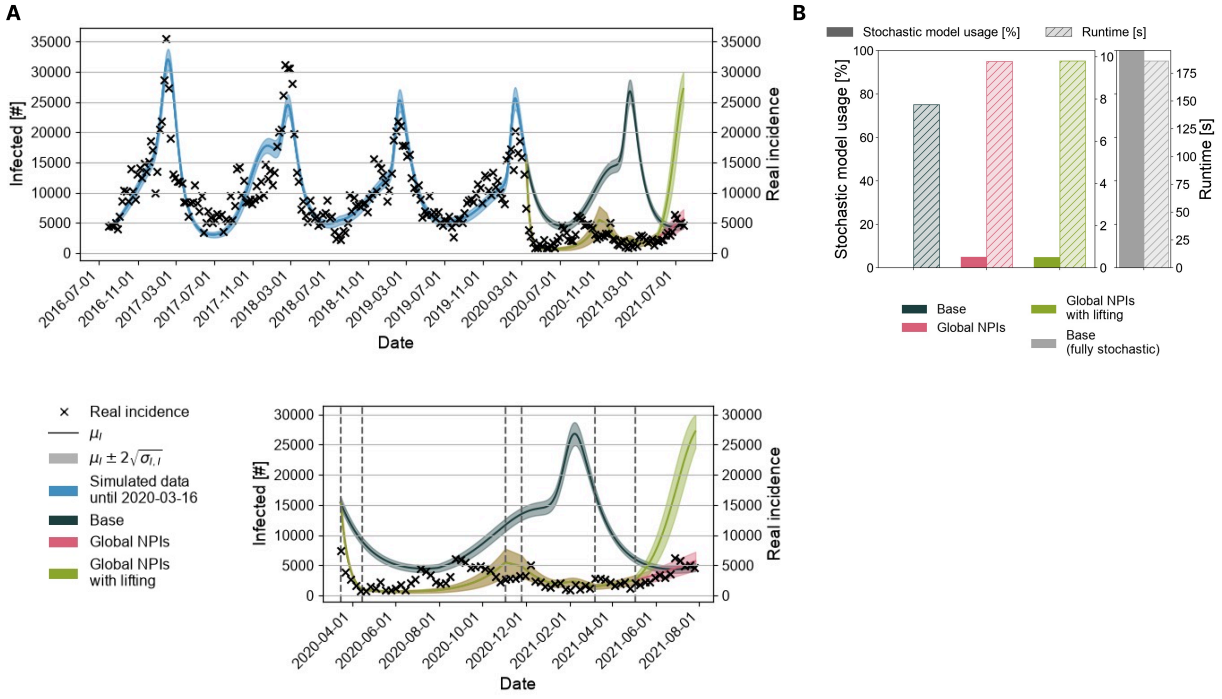


Figure 7: Simulation outcomes of the hybrid model in three different scenarios for the evolution of ILI incidence in Germany. A: Simulated prevalence trajectories of the hybrid model compared to real ILI incidence. The shown incidence corresponds to the reported weekly number of new infections scaled to match the modeled population size. Shown is the simulated mean number of infected (solid line) and twice the standard deviation (shaded area). The scenarios only differ from 16th March 2020 onwards when either no transmission rate dampings (Base), five dampings of varying strength (Global NPIs) or five dampings plus a sixth one that fully lifts the previous dampings from 3rd May 2021 onwards (Global NPIs total lifting) are applied. **B:** Runtime and relative number of time steps modeled with the stochastic formulation in the temporal hybrid model for all three scenarios compared to the Base scenario modeled fully stochastically.

In a second step, we extended the temporal-hybrid model for ILI to a spatio-temporal metapopulation model comprising four regions (Fig. 8A), consistent with the spatially resolved data reported by [53]. Unlike the global model, this regional model incorporates region-dependent transmission rates, enabling regionally heterogeneous NPIs. Furthermore, it integrates mobility patterns via spatial transition rates that were derived from a trip data set comprising activity-dependent daily trips between 400 German counties [56]. Based on [57], we considered only work-related trips. The spatial transition rate $\kappa_z^{(k,l)}$, $z \in \{S, I, R\}$, from region k to region l, $k \neq l$, is given by

$$\kappa_z^{(k,l)} = \frac{n_{trips}^{(k,l)} + n_{trips}^{(l,k)}}{N^{(k)}},$$

with $n_{trips}^{(k,l)}, n_{trips}^{(l,k)}$ the daily number of work-related trips from region k to region l and vice versa; and $N^{(k)}$ the

population size of region k. The spatial transition rates govern movement of individuals between regions (Fig. 8B) and thus mediate inter-region transmission.

In addition to the three scenarios defined for the global model (Base, Global NPIs, Global NPIs total lifting), we considered two supplementary scenarios that explicitly account for regional disparities in interventions. In these settings, we calibrated the regional transmission rates and initial mean values such that infection dynamics until 16th March 2020 match the spatially-resolved reported incidence data. We specifically considered the southern region and either implemented no intervention in this region or implemented a 10 % stricter intervention set than in the other regions. More precisely, we considered the following two settings.

- No NPIs in the South: The global damping factors $d^{(1)}, \ldots, d^{(6)} \in \mathbb{R}$ are applied to regions 1, 2 and 4, while region 3 (South) remains unaffected by interventions and transmission dynamics in that region continue unchanged from 9th March 2020.

- Stricter NPIs in the South: The global damping factors are applied in region 1, 2 and 4, while in region 3 10 % stricter dampings are applied during the intervals $[t_{d^{(1)}}, t_{d^{(2)}})$, $[t_{d^{(3)}}, t_{d^{(4)}})$ and $[t_{d^{(4)}}, t_{d^{(5)}})$.

As in the global model, the runtime of the regional model depends on the number of time steps modeled stochastically. Scenarios with a higher proportion of time steps modeled stochastically exhibit correspondingly longer runtimes (Fig. 8C).

Incidence trajectories in the four regions reveal regionally heterogeneous patterns in ILI dynamics (Fig. 9). The baseline, global NPIs and global NPIs with total lifting scenarios produce similar trajectories to those observed in the global model. Among these, the global NPIs scenario without full lifting aligns best with reported incidence estimates. However, quantitative differences in peak prevalence and cumulative infections can be observed between regions, with region Middle (West) exhibiting the highest overall prevalence level. This may be attributed to its higher population density, resulting in increased contact rates, thereby enhancing transmission risk.

The local scenarios (No NPIs in the South, Stricter NPIs in the South) reveal that regional intervention policies have non-local effects. In the no local interventions scenario, region 3 experiences an epidemic wave similar to the baseline scenario. While we only see slightly increased infection levels in the North-Western and Eastern regions, we observe a relatively large number of infections in the Middle-Western region although interventions are in place. More precisely, besides region 3, local absence of interventions has the most pronounced effect in region 4 which experiences a second small infection wave from February to April 2021, following the wave in November 2020. This behavior is driven by the relatively high number of spatial transitions between region 3 and region 4, yielding sustained import of cases. In contrast, the scenario with 10 % stricter NPIs in region 3 results in only marginal reductions in infection prevalence across all regions.

4. Discussion

In this study, we developed a spatio-temporal hybrid framework that allows each region of an epidemiological metapopulation model to switch independently between stochastic ensemble simulations and moment equations. The central methodological contribution is the use of ensemble-level statistics to guide local model choice. By retaining means, variances, and covariances during deterministic simulation, the framework accounts for epidemic variability beyond mean dynamics.

First, we quantified the computational cost of stochastic ensembles and the moment-closure approximation by examining their scaling behavior in three different settings. This analysis revealed that as the

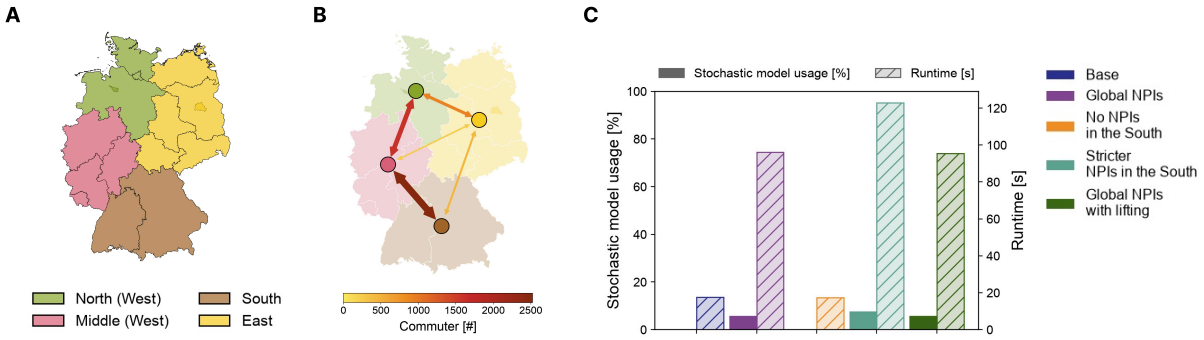


Figure 8: Simulation outcomes of the hybrid model in five different scenarios for the spatially resolved evolution of ILI incidence in Germany. A: Mapping of German federal states to modeled regions. **B:** Visualization of spatial transition between regions. **C:** Runtime and relative number of time steps modeled with the stochastic formulation in the spatio-temporal hybrid model for all five scenarios.

number of regions increases, the runtime advantage of the moment-closure approximation over stochastic simulations diminishes. Conversely, larger total population sizes enhance the computational advantage of the moment-closure approximation compared to stochastic simulations. We systematically assessed the accuracy of the moment-closure approximation and used these results to formulate and compare switching criteria based on mean infection levels, relative variability, and the effective reproduction number. Finally, the application of the spatio-temporal-hybrid model to seasonal ILI demonstrates how regional interventions influence global dynamics and highlights the framework's potential for real-world epidemic forecasting. The seasonality function as well as applied dampings may lead to discontinuous transmission rates. Since dampings and season changes occurred only at full days, these discontinuities coincided with step boundaries and did therefore not cause integration problems. An alternative possible solution would be using sufficiently smooth interpolating transitions as discussed in [58]. Due to computational constraints, we only considered one hundredth of Germany's total population size and further assumed the average number of contacts to be proportional to the population size in a region. This assumption leads to reduced fluctuations in compartment sizes when increasing the population size, e.g. to the full population of Germany, which in turn influences the output of (switching) condition functions. Alternatively, regional transmission rates could be scaled by local population sizes, ensuring a constant average number of contacts.

The presented framework extends our previous temporal and spatial hybridization approaches [42] by combining both forms of adaptation and applying switching criteria to summary statistics of the stochastic ensemble. Previous hybrid approaches for infectious disease dynamics have combined stochastic and deterministic descriptions in time, space, or both [40, 41, 35, 37, 36]. Our emphasis is on linking the choice of representation to an empirical assessment of moment-closure accuracy, rather than relying solely on compartment counts in an individual realization. This enables the switching decision to account for variability across possible epidemic outcomes. The comparison of alternative criteria also demonstrates that their suitability depends on the dynamical regime and the desired balance between accuracy and computational cost. The conditions considered in this study use the moment-closure approximation if the mean number of infected is smaller than one. This condition is fulfilled in complete extinction settings, but also in scenarios with high extinction probability and a few surviving infections. Although the latter is not particularly likely for large population sizes, to explicitly exclude such scenarios from switching conditions, the cumulative size of the infected compartment could be used to inform switching conditions.

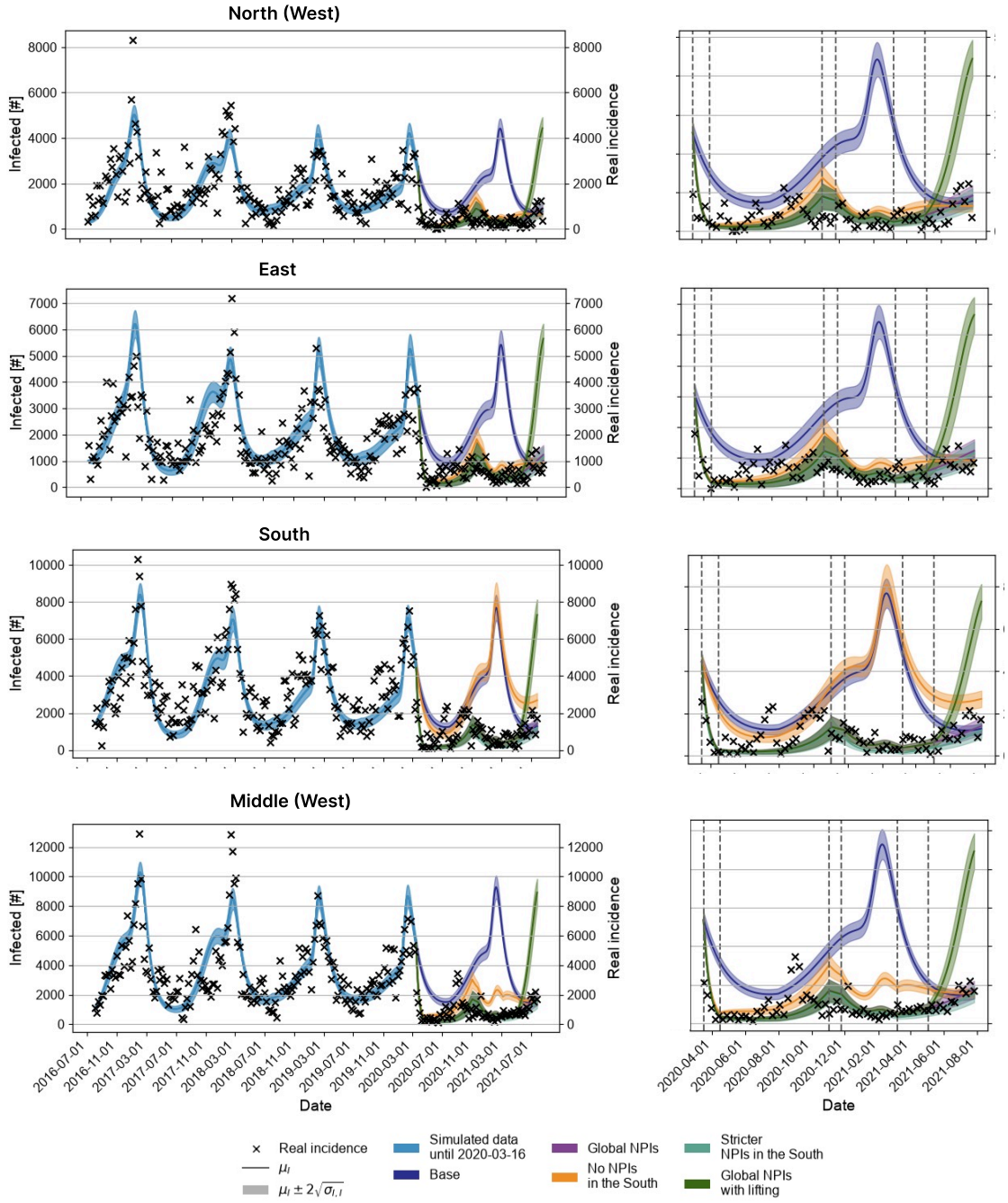


Figure 9: Simulation outcomes of the hybrid model in five different scenarios for the spatially resolved evolution of ILI incidence in Germany. From 16th March 2020 onward no dampings (Base), five (Global NPIs) or six (Global NPIs with lifting) identical dampings in all four regions, regionally heterogeneous dampings (Stricter NPIs in the South) or regionally heterogeneous lifting of dampings (No NPIs in the South) are applied. Shown is the whole modeled time frame (1st August 2016 - 27th July 2021) for each region and a zoomed in frame from the potential first damping time point until simulation end.

Our approach further differs from hybrid methods that retain a reduced master equation for selected components of the system [32, 59, 60]. Such methods can be effective when the retained stochastic state

space is sufficiently small, but this space may remain large for epidemiological compartments. Moment equations reduce computational effort in regimes where the closure provides an adequate approximation. Conversion and exchange rules connect the two representations, although reconstructing ensembles from a finite set of moments and approximating dependencies across their interface introduce additional errors that must be considered alongside moment-closure error. Future work should incorporate covariance contributions from incoming subpopulations and quantify the additional noise introduced by sampling variances uniformly within defined boundaries. Furthermore, extensions to non-polynomial propensities should be implemented (e.g., based on [61]) to support common infection rates.

We also leave for future work to extend the SIR- and SIRS-type models by an incidence compartment describing the flow from susceptible to infected. Such a compartment would circumvent using prevalence as a proxy for reported incidence, thereby facilitating the incorporation of and comparison with real-world data.

Concluding, our study highlights the potential of hybrid stochastic-deterministic models to balance the trade-off between accuracy and computational complexity. While we demonstrated the applicability and performance of our framework in synthetic settings as well as for real-world scenario analysis, applying it to computationally intensive parameter estimation tasks offers further potential to reduce runtime and energy consumption.

Acknowledgments

This work was supported by the Initiative and Networking Fund of the Helmholtz Association (grant agreement number KA1-Co-08, Project LOKI-Pandemics). It was furthermore supported by the German Federal Ministry of Education and Research and the German Federal Ministry of Research, Technology and Space under grant agreement 031L0325A (Project TwinChain). TwinChain is part of the Modeling Network for Severe Infectious Diseases (MONID). Additionally, this work was supported by the European Union via the ERC grant INTEGRATE, grant agreement number 101126146, and under Germany's Excellence Strategy by the Deutsche Forschungsgemeinschaft (DFG, German Research Foundation) (EXC 2047—390685813, EXC 2151—390873048, and 524747443), and by the University of Bonn via the Schlegel Professorship of J.H.

Declaration of competing interest

The authors declare to not have any conflict of interest.

Data availability

The developed models as well as all simulation code for this study are implemented within the MEmilio software framework and publicly available at `https://github.com/jubicker/memilio/tree/hybrid2`. Visualized simulation data can be shared upon request.

CRediT authorship contribution statement

Julia Bicker: Writing – Review & Editing, Writing – Original Draft, Conceptualization, Data Curation, Formal Analysis, Investigation, Methodology, Software, Validation, Visualization. **Kilian Volmer:** Writing – Review & Editing, Conceptualization, Software, Validation. **Jan Hasenauer:** Writing – Review & Editing, Conceptualization, Funding Acquisition, Project Administration, Supervision, Validation. **Martin**

J. Kühn: Writing – Review & Editing, Conceptualization, Funding Acquisition, Project Administration, Supervision, Validation.

References

[1] European Centre for Disease Prevention and Control, Public health and social measures for health emergencies and pandemics in the EU/EEA: recommendations for strengthening preparedness planning, Tech. rep., European Centre for Disease Prevention and Control (2024). doi:10.2900/253991.

[2] S. Khailaie, T. Mitra, A. Bandyopadhyay, M. Schips, P. Mascheroni, P. Vanella, B. Lange, S. C. Binder, M. Meyer-Hermann, Development of the reproduction number from coronavirus SARS-CoV-2 case data in Germany and implications for political measures, BMC medicine 19 (1) (2021) 1–16.

[3] O. N. Bjørnstad, K. Shea, M. Krzywinski, N. Altman, The SEIRS model for infectious disease dynamics, Nature Methods 17 (6) (2020) 557–558. doi:10.1038/s41592-020-0856-2.
URL https://www.nature.com/articles/s41592-020-0856-2

[4] G. Giordano, F. Blanchini, R. Bruno, P. Colaneri, A. Di Filippo, A. Di Matteo, M. Colaneri, Modelling the COVID-19 epidemic and implementation of population-wide interventions in Italy, Nature Medicine 26 (6) (2020) 855–860. doi:10.1038/s41591-020-0883-7.

[5] J. Arino, P. van den Driessche, A multi-city epidemic model, Mathematical Population Studies 10 (3) (2003) 175–193. doi:10.1080/08898480306720.

[6] C. Cosner, J. Beier, R. Cantrell, D. Impoinvil, L. Kapitanski, M. Potts, A. Troyo, S. Ruan, The effects of human movement on the persistence of vector-borne diseases, Journal of Theoretical Biology 258 (4) (2009) 550–560. doi:https://doi.org/10.1016/j.jtbi.2009.02.016.

[7] J. Wang, X. Wang, J. Wu, Inferring metapopulation propagation network for intra-city epidemic control and prevention, in: Proceedings of the 24th ACM SIGKDD International Conference on Knowledge Discovery & Data Mining, KDD '18, Association for Computing Machinery, New York, NY, USA, 2018, p. 830–838. doi:10.1145/3219819.3219865.

[8] D. T. Citron, C. A. Guerra, A. J. Dolgert, S. L. Wu, J. M. Henry, H. M. S. C., D. L. Smith, Comparing metapopulation dynamics of infectious diseases under different models of human movement, Proceedings of the National Academy of Sciences 118 (18) (2021) e2007488118. doi:10.1073/pnas.2007488118.

[9] J. Liu, G. P. Ong, V. J. Pang, Modelling effectiveness of COVID-19 pandemic control policies using an Area-based SEIR model with consideration of infection during interzonal travel, Transportation Research Part A: Policy and Practice 161 (2022) 25–47. doi:10.1016/j.tra.2022.05.003.

[10] J. Bicker, C. Gerstein, D. Kerkmann, S. Korf, R. Schmieding, A. Wendler, H. Zunker, D. Abele, M. Betz, K. Nguyen, L. Plötzke, K. Volmer, A. Schmidt, N. Waßmuth, P. Lenz, D. Richter, H. Tritzschak, R. Hannemann-Tamas, J. Litz, P. Johannssen, M. Borges, A. Jungklaus, M. Heger, A. Lange, E. Kluth, K. Rack, V. Wieland, J. Arruda, S. Binder, M. Klitz, M. Siggel, M. Dahmen, A. Basermann, M. Meyer-Hermann, J. Hasenauer, M. J. Kühn, Memilio – a high performance modular epidemics simulation software for multi-scale and comparative simulations of infectious disease dynamics, Scientific Reports 16 (1) (2026) 26950. doi:10.1038/s41598-026-66481-6.

[11] H. Zunker, R. Schmieding, J. Hasenauer, M. J. Kühn, Efficient numerical computation of traveler states in explicit mobility-based metapopulation models: Mathematical theory and application to epidemics, Mathematics and Computers in Simulation 251 (2027) 798–812. doi:10.1016/j.matcom.2026.08.029.

[12] D. Kerkmann, S. Korf, K. Nguyen, D. Abele, A. Schengen, C. Gerstein, J. H. Göbbert, A. Basermann, M. J. Kühn, M. Meyer-Hermann, Agent-based modeling for realistic reproduction of human mobility and contact behavior to evaluate test and isolation strategies in epidemic infectious disease spread, Computers in Biology and Medicine 193 (2025) 110269. doi:https://doi.org/10.1016/j.compbiomed.2025.110269.
URL https://doi.org/10.1016/j.compbiomed.2025.110269

[13] C. C. Kerr, R. M. Stuart, D. Mistry, R. G. Abeysuriya, K. Rosenfeld, G. R. Hart, R. C. Núñez, J. A. Cohen, P. Selvaraj, B. Hagedorn, L. George, M. Jastrzebski, A. S. Izzo, G. Fowler, A. Palmer, D. Delport, N. Scott, S. L. Kelly, C. S. Bennette, B. G. Wagner, S. T. Chang, A. P. Oron, E. A. Wenger, J. Panovska-Griffiths, M. Famulare, D. J. Klein, Covasim: An agent-based model of COVID-19 dynamics and interventions, PLOS Computational Biology 17 (7) (2021) 1–32. doi:10.1371/journal.pcbi.1009149.
URL https://doi.org/10.1371/journal.pcbi.1009149

[14] A. J. Shattock, E. A. Le Rutte, R. P. Dünner, S. Sen, S. L. Kelly, N. Chitnis, M. A. Penny, Impact of vaccination and non-pharmaceutical interventions on SARS-CoV-2 dynamics in Switzerland, Epidemics 38 (2022) 100535. doi:10.1016/j.epidem.2021.100535.
URL https://doi.org/10.1016/j.epidem.2021.100535

[15] D. L. Chao, M. E. Halloran, V. J. Obenchain, I. M. L. Jr, FluTE, a publicly available stochastic influenza epidemic simulation model, PLOS Computational Biology 6 (1) e1000656. doi:10.1371/journal.pcbi.1000656.

[16] M. J. Kühn, D. Abele, T. Mitra, W. Koslow, M. Abedi, K. Rack, M. Siggel, S. Khailaie, M. Klitz, S. Binder, L. Spataro, J. Gilg, J. Kleinert, M. Häberle, L. Plötzke, C. D. Spinner, M. Stecher, X. X. Zhu, A. Basermann, M. Meyer-Hermann, Assessment of effective mitigation and prediction of the spread of SARS-CoV-2 in Germany using demographic information and spatial resolution, Mathematical Biosciences (2021) 108648doi:https://doi.org/10.1016/j.mbs.2021.108648.
URL https://doi.org/10.1016/j.mbs.2021.108648

[17] G. Rozhnova, C. H. Van Dorp, P. Bruijning-Verhagen, M. C. J. Bootsma, J. H. H. M. Van De Wijgert, M. J. M. Bonten, M. E. Kretzschmar, Model-based evaluation of school- and non-school-related measures to control the COVID-19 pandemic, Nature Communications 12 (1) (Mar. 2021). doi:10.1038/s41467-021-21899-6.

[18] I. Krishnarajah, A. Cook, G. Marion, G. Gibson, Novel moment closure approximations in stochastic epidemics, Bulletin of Mathematical Biology 67 (4) (2005) 855–873. doi:10.1016/j.bulm.2004.11.002.

[19] S. Winkelmann, J. Zonker, C. Schütte, N. D. Conrad, Mathematical modeling of spatio-temporal population dynamics and application to epidemic spreading, Mathematical Biosciences 336 (2021) 108619. doi:https://doi.org/10.1016/j.mbs.2021.108619.

[20] M. A. Achterberg, P. Van Mieghem, Moment closure approximations of susceptible-infected-susceptible epidemics on adaptive networks, Phys. Rev. E 106 (2022) 014308. doi:10.1103/PhysRevE.106.014308.

[21] P. J. Hurtado, A. S. Kirosingh, Generalizations of the 'Linear Chain Trick': incorporating more flexible dwell time distributions into mean field ODE models, Journal of Mathematical Biology 79 (5) (Oct. 2019). doi:10.1007/s00285-019-01412-w.

[22] L. Plötzke, A. Wendler, R. Schmieding, M. J. Kühn, Revisiting the linear chain trick in epidemiological models: Implications of underlying assumptions for numerical solutions, Mathematics and Computers in Simulation 239 (2026) 823–844. doi:https://doi.org/10.1016/j.matcom.2025.07.045.

[23] D. T. Gillespie, Exact stochastic simulation of coupled chemical reactions, The Journal of Physical Chemistry 81 (25) (1977) 2340–2361. doi:10.1021/j100540a008.
URL https://doi.org/10.1021/j100540a008

[24] D. A. McQuarrie, Stochastic approach to chemical kinetics, Journal of applied probability 4 (3) (1967) 413–478.

[25] S. Engblom, Computing the moments of high dimensional solutions of the master equation, Applied Mathematics and Computation 180 (2) (2006) 498–515. doi:10.1016/j.amc.2005.12.032.

[26] C. H. Lee, K.-H. Kim, P. Kim, A moment closure method for stochastic reaction networks, The Journal of Chemical Physics 130 (13) (2009) 134107. doi:10.1063/1.3103264.

[27] C. Gillespie, Moment-closure approximations for mass-action models, IET Systems Biology 3 (1) (2009) 52–58. doi:10.1049/iet-syb:20070031.

[28] A. Singh, J. P. Hespanha, Lognormal Moment Closures for Biochemical Reactions, in: Proceedings of the 45th IEEE Conference on Decision and Control, IEEE, San Diego, CA, USA, 2006, pp. 2063–2068. doi:10.1109/CDC.2006.376994.

[29] L. Bronstein, H. Koeppl, A variational approach to moment-closure approximations for the kinetics of biomolecular reaction networks, The Journal of Chemical Physics 148 (1) (2018) 014105. doi:10.1063/1.5003892.

[30] A. Singh, J. P. Hespanha, A Derivative Matching Approach to Moment Closure for the Stochastic Logistic Model, Bulletin of Mathematical Biology 69 (6) (2007) 1909–1925. doi:10.1007/s11538-007-9198-9.

[31] A. Singh, J. P. Hespanha, Approximate Moment Dynamics for Chemically Reacting Systems, IEEE Transactions on Automatic Control 56 (2) (2011) 414–418. doi:10.1109/TAC.2010.2088631.

[32] J. Hasenauer, V. Wolf, A. Kazeroonian, F. J. Theis, Method of conditional moments (MCM) for the Chemical Master Equation: A unified framework for the method of moments and hybrid stochastic-deterministic models, Journal of Mathematical Biology 69 (3) (2014) 687–735. doi:10.1007/s00285-013-0711-5.

[33] T. Yoneyama, S. Das, M. Krishnamoorthy, A hybrid model for disease spread and an application to the SARS pandemic, Journal of Artificial Societies and Social Simulation 15 (1) (2012) 5. doi:10.18564/jasss.1782.

[34] S. Kasereka, N. Kasoro, A. P. Chokki, A hybrid model for modeling the spread of epidemics: Theory and simulation, in: 2014 4th International Symposium ISKO-Maghreb: Concepts and Tools for knowledge Management (ISKO-Maghreb), IEEE, Algiers, Algeria, 2014, pp. 1–7. doi:10.1109/ISKO-Maghreb.2014.7033457.

[35] R. A. Bradhurst, S. E. Roche, I. J. East, P. Kwan, M. G. Garner, A hybrid modeling approach to simulating foot-and-mouth disease outbreaks in Australian livestock, Frontiers in Environmental Science 3 (Mar. 2015). doi:10.3389/fenvs.2015.00017.

[36] I. Bostanci, T. Conrad, Integrating agent-based and compartmental models for infectious disease modeling: A novel hybrid approach, Journal of Artificial Societies and Social Simulation 28 (1) (2025) 5. doi:10.18564/jasss.5567.

[37] K. Kehrer, M. Weiser, T. Conrad, Hybrid PDE–ODE models for efficient simulation of infection spread in epidemiology, Proceedings of the Royal Society A: Mathematical, Physical and Engineering Sciences 481 (2305) (2025) 20240421. doi:10.1098/rspa.2024.0421.

[38] K. Kehrer, T. O. F. Conrad, A hybrid ABM-PDE framework for real-world infectious disease simulations, Applied Mathematical Modelling 162 (2027) 117173. doi:10.1016/j.apm.2026.117173.

[39] J. Kwak, M. H. Lees, C. C. Ooi, W. Cai, Hybrid epidemic simulation framework coupling equation-based and individual-based models, arxiv (2026). doi:10.48550/arXiv.2609.35162.

[40] G. V. Bobashev, D. M. Goedecke, Feng Yu, J. M. Epstein, A hybrid epidemic model: Combining the advantages of agent-based And Equation-based approaches, in: 2007 Winter Simulation Conference, IEEE, Washington, DC, USA, 2007, pp. 1532–1537. doi:10.1109/WSC.2007.4419767.

[41] E. Hunter, B. Mac Namee, J. Kelleher, A hybrid agent-based and equation based model for the spread of infectious diseases, Journal of Artificial Societies and Social Simulation 23 (4) (2020) 14. doi:10.18564/jasss.4421.

[42] J. Bicker, R. Schmieding, M. Meyer-Hermann, M. J. Kühn, Hybrid metapopulation agent-based epidemiological models for efficient insight on the individual scale: A contribution to green computing, Infectious Disease Modelling 10 (2) (2025) 571–590. doi:https://doi.org/10.1016/j.idm.2024.12.015.

[43] D. F. Anderson, A modified next reaction method for simulating chemical systems with time dependent propensities and delays, The Journal of Chemical Physics 127 (21) (2007) 214107. doi:10.1063/1.2799998.
URL https://pubs.aip.org/aip/jcp/article/349528

[44] J. Hespanha, Moment closure for biochemical networks, in: 2008 3rd International Symposium on Communications, Control and Signal Processing, IEEE, St. Julian's, Malta, 2008, pp. 142–147. doi:10.1109/ISCCSP.2008.4537208.

[45] D. Schnoerr, G. Sanguinetti, R. Grima, Comparison of different moment-closure approximations for stochastic chemical kinetics, The Journal of Chemical Physics 143 (18) (2015) 185101. doi:10.1063/1.4934990.

[46] K. Ahnert, M. Mulansky, Odeint – Solving Ordinary Differential Equations in C++, AIP Conference Proceedings 1389 (1) (2011) 1586–1589. doi:10.1063/1.3637934.
URL https://doi.org/10.1063/1.3637934

[47] J. J. Bull, K. Koelle, R. Antia, Waning immunity drives respiratory virus evolution and reinfection, Evolution, Medicine, and Public Health 13 (1) (2025) 101–110. doi:10.1093/emph/eoaf002.

[48] V. N. Petrova, C. A. Russell, The evolution of seasonal influenza viruses, Nature Reviews Microbiology 16 (1) (2018) 47–60. doi:10.1038/nrmicro.2017.118.

[49] M. Moriyama, W. J. Hugentobler, A. Iwasaki, Seasonality of Respiratory Viral Infections, Annual Review of Virology 7 (1) (2020) 83–101. doi:10.1146/annurev-virology-012420-022445.

[50] S. Edlund, J. Kaufman, J. Lessler, J. Douglas, M. Bromberg, Z. Kaufman, R. Bassal, G. Chodick, R. Marom, V. Shalev, et al., Comparing three basic models for seasonal influenza, Epidemics 3 (3-4) (2011) 135–142. doi:10.1016/j.epidem.2011.04.002.

[51] S. E. Morris, H. Q. Nguyen, C. G. Grijalva, K. E. Hanson, Y. Zhu, J. E. Biddle, J. K. Meece, N. B. Halasa, J. D. Chappell, A. M. Mellis, C. Reed, M. Biggerstaff, E. A. Belongia, H. K. Talbot, M. A. Rolfes, Influenza virus shedding and symptoms: Dynamics and implications from a multiseason household transmission study, PNAS Nexus 3 (9) (2024) pgae338. doi:10.1093/pnasnexus/pgae338.

[52] D. K. M. Ip, L. L. H. Lau, N. H. L. Leung, V. J. Fang, K.-H. Chan, D. K. W. Chu, G. M. Leung, J. S. M. Peiris, T. M. Uyeki, B. J. Cowling, Viral Shedding and Transmission Potential of Asymptomatic and Paucisymptomatic Influenza Virus Infections in the Community, Clinical Infectious Diseases 64 (6) (2017) 736–742. doi:10.1093/cid/ciw841.

[53] U. Buchholz, A.-S. Lehfeld, A. Loenenbach, K. Prahm, U. Preuß, A. Stepanovich-Falke, W. Haas, GrippeWeb - Daten des Wochenberichts (Aug. 2026). doi:10.5281/zenodo.22024280.
URL https://robert-koch-institut.github.io/GrippeWeb_Daten_des_Wochenberichts

[54] Y. Schälte, E. Klinger, E. Alamoudi, J. Hasenauer, pyABC: Efficient and robust easy-to-use approximate Bayesian computation, Journal of Open Source Software 7 (74) (2022) 4304. doi:10.21105/joss.04304.
URL https://doi.org/10.21105/joss.04304

[55] A3M Global Monitoring GmbH, COVID-19 pandemic - Germany, https://global-monitoring.com/gm/page/events/epidemic-0001937.eP207vO5rIwe.html, https://global-monitoring.com/gm/page/events/epidemic-0001937.eP207vO5rIwe.html, accessed: 10 Aug 2026 (2025).

[56] M. Kühn, A. Schengen, T. Mocanu, J. Joshi, Vorläufige bundesweite Verkehrsströme (Mar. 2023).
URL https://mobilithek.info/offers/573360269906817024

[57] H. Zunker, R. Schmieding, D. Kerkmann, A. Schengen, S. Diexer, R. Mikolajczyk, M. Meyer-Hermann, M. J. Kühn, Novel travel time aware metapopulation models and multi-layer waning immunity for late-phase epidemic and endemic scenarios, PLOS Computational Biology 20 (12) (Dez 2024). doi:10.1371/journal.pcbi.1012630.
URL https://doi.org/10.1371/journal.pcbi.1012630

[58] A. Wendler, J. Hasenauer, M. Kühn, Higher order schemes for the numerical solution of integro-differential equation-based age-of-infection models with time-dependent contact ratesSubmitted. (2026).

[59] S. Menz, J. C. Latorre, C. Schütte, W. Huisinga, Hybrid Stochastic–Deterministic Solution of the Chemical Master Equation, Multiscale Modeling & Simulation 10 (4) (2012) 1232–1262. doi:10.1137/110825716.

[60] T. Jahnke, On Reduced Models for the Chemical Master Equation, Multiscale Modeling & Simulation 9 (4) (2011) 1646–1676. doi:10.1137/110821500.

[61] A. Kazeroonian, F. J. Theis, J. Hasenauer, Modeling of stochastic biological processes with non-polynomial propensities using non-central conditional moment equation, in: Proceedings of the 19th IFAC World Congress, Vol. 19, Cape Town, South Africa, 2014, pp. 1729–1735. doi:10.3182/20140824-6-ZA-1003.02298.
URL http://dx.doi.org/10.3182/20140824-6-ZA-1003.02298

[62] Statistische Ämter des Bundes und der Länder, Bevölkerung nach Geschlecht und Altersgruppen (17) – Stichtag 31.12. – regionale Tiefe: Gemeinden, https://www.regionalstatistik.de/genesis/online?operation=table&code=12411-02-03-5, accessed: 2025-04-22 (2025).

[63] J. Bicker, D. Kerkmann, S. A. Korf, L. Plötzke, R. Schmieding, A. C. Wendler, H. Zunker, K. Nguyen, D. Abele, C. Gerstein, P. Lenz, M. F. Betz, A. Schmidt, R. Hannemann-Tamas, K. Volmer, N. Waßmuth, H. Tritzschak, D. Richter, M. Heger, A. Basermann, M. Meyer-Hermann, J. Hasenauer, M. J. Kühn, MEmilio v2.3.0 - A high performance Modular EpideMIcs simuLatIOn software (2026).
URL https://doi.org/10.5281/zenodo.18929098

Supplementary Information

Appendix A. Moment equations

For $l = 1, \ldots, n_R$, the evolution equations for the mean of the SIRS-type metapopulation model are given by

$$\frac{d\mu_{\iota(S,l)}}{dt} = -\lambda^{(l)} \cdot \left(\mu_{\iota(S,l)}\mu_{\iota(I,l)} + \mathbb{E}\left[(X_S^{(l)} - \mu_{\iota(S,l)})(X_I^{(l)} - \mu_{\iota(I,l)})\right]\right) + \alpha\mu_{\iota(R,l)} + \sum_{\substack{k=1 \\ k\neq l}}^{n_R}(\kappa_S^{(k,l)}\mu_{\iota(S,k)} - \kappa_S^{(l,k)}\mu_{\iota(S,l)})$$

$$\frac{d\mu_{\iota(I,l)}}{dt} = \lambda^{(l)} \cdot \left(\mu_{\iota(S,l)}\mu_{\iota(I,l)} + \mathbb{E}\left[(X_S^{(l)} - \mu_{\iota(S,l)})(X_I^{(l)} - \mu_{\iota(I,l)})\right]\right) - \gamma\mu_{\iota(I,l)} + \sum_{\substack{k=1 \\ k\neq l}}^{n_R}(\kappa_I^{(k,l)}\mu_{\iota(I,k)} - \kappa_I^{(l,k)}\mu_{\iota(I,l)})$$

$$\frac{d\mu_{\iota(R,l)}}{dt} = \gamma\mu_{\iota(I,l)} - \alpha\mu_{\iota(R,l)} + \sum_{\substack{k=1 \\ k\neq l}}^{n_R}(\kappa_R^{(k,l)}\mu_{\iota(R,k)} - \kappa_R^{(l,k)}\mu_{\iota(R,l)})$$

The ODE system for the variances $\sigma_{\iota(z,l),\iota(z,l)} = \mathbb{E}[(X_z^{(l)} - \mu_{\iota(z,l)})^2]$, $z \in \{S, I, R\}$, is given by

$$\begin{aligned}
\frac{d\sigma_{\iota(S,l),\iota(S,l)}}{dt} &= \lambda^{(l)}\mu_{\iota(S,l)}\mu_{\iota(I,l)} + \alpha\mu_{\iota(R,l)} + \sum_{\substack{k=1 \\ k\neq l}}^{n_R}(\kappa_S^{(l,k)}\mu_{\iota(S,l)} + \kappa_S^{(k,l)}\mu_{\iota(S,k)}) \\
&\quad - 2\lambda^{(l)}\Big(\mu_{\iota(I,l)}\sigma_{\iota(S,l),\iota(S,l)} + \mu_{\iota(S,l)}\mathbb{E}[(X_S^{(l)} - \mu_{\iota(S,l)})(X_I^{(l)} - \mu_{\iota(I,l)})]\Big) \\
&\quad + 2\alpha\mathbb{E}[(X_S^{(l)} - \mu_{\iota(S,l)})(X_R^{(l)} - \mu_{\iota(R,l)})] \\
&\quad + 2\sum_{\substack{k=1 \\ k\neq l}}^{n_R}\Big(-\kappa_S^{(l,k)}\sigma_{\iota(S,l),\iota(S,l)} + \kappa_S^{(k,l)}\mathbb{E}[(X_S^{(l)} - \mu_{\iota(S,l)})(X_S^{(k)} - \mu_{\iota(S,k)})]\Big) \\
&\quad + \lambda^{(l)}\mathbb{E}[(X_S^{(l)} - \mu_{\iota(S,l)})(X_I^{(l)} - \mu_{\iota(I,l)})] - 2\lambda^{(l)}\mathbb{E}[(X_S^{(l)} - \mu_{\iota(S,l)})^2(X_I^{(l)} - \mu_{\iota(I,l)})] \\
\frac{d\sigma_{\iota(I,l),\iota(I,l)}}{dt} &= \lambda^{(l)}\mu_{\iota(S,l)}\mu_{\iota(I,l)} + \gamma\mu_{I^{(l)}} + \sum_{\substack{k=1 \\ k\neq l}}^{n_R}(\kappa_I^{(l,k)}\mu_{\iota(I,l)} + \kappa_I^{(k,l)}\mu_{\iota(I,k)}) \\
&\quad + 2\lambda^{(l)}\Big(\mu_{\iota(I,l)}\mathbb{E}[(X_S^{(l)} - \mu_{\iota(S,l)})(I^{(l)} - \mu_{\iota(I,l)})] + \mu_{\iota(S,l)}\sigma_{\iota(I,l),\iota(I,l)}\Big) - 2\gamma\sigma_{\iota(I,l),\iota(I,l)} \\
&\quad + 2\sum_{\substack{k=1 \\ k\neq l}}^{n_R}\Big(-\kappa_I^{(l,k)}\sigma_{\iota(I,l),\iota(I,l)} + \kappa_I^{(k,l)}\mathbb{E}[(X_I^{(l)} - \mu_{\iota(I,l)})(X_I^{(k)} - \mu_{\iota(I,k)})]\Big) \\
&\quad + \lambda^{(l)}\mathbb{E}[(X_S^{(l)} - \mu_{\iota(S,l)})(X_I^{(l)} - \mu_{\iota(I,l)})] + 2\lambda^{(l)}\mathbb{E}[(X_S^{(l)} - \mu_{\iota(S,l)})(X_I^{(l)} - \mu_{\iota(I,l)})^2] \\
\frac{d\sigma_{\iota(R,l),\iota(R,l)}}{dt} &= \gamma\mu_{\iota(I,l)} + \alpha\mu_{\iota(R,l)} + \sum_{\substack{k=1 \\ k\neq l}}^{n_R}(\kappa_R^{(l,k)}\mu_{\iota(R,l)} + \kappa_R^{(k,l)}\mu_{\iota(R,k)}) + 2\gamma\mathbb{E}[(X_I^{(l)} - \mu_{\iota(I,l)})(X_R^{(l)} - \mu_{\iota(R,l)})] \\
&\quad - 2\alpha\sigma_{\iota(R,l),\iota(R,l)} + 2\sum_{\substack{k=1 \\ k\neq l}}^{n_R}\Big(-\kappa_R^{(l,k)}\sigma_{\iota(R,l),\iota(R,l)} + \kappa_R^{(k,l)}\mathbb{E}[(X_R^{(l)} - \mu_{\iota(R,l)})(X_R^{(k)} - \mu_{\iota(R,k)})]\Big)
\end{aligned}$$

In general, we denote the m-th central moment of the SIRS-type metapopulation model as

$$M_{i_S^{(1)},i_I^{(1)},i_R^{(1)},\ldots,i_R^{(n_R)}} = \mathbb{E}[(X_S^{(1)} - \mu_{\iota(S,1)})^{i_S^{(1)}}(X_I^{(1)} - \mu_{\iota(I,1)})^{i_I^{(1)}}(X_R^{(1)} - \mu_{\iota(R,1)})^{i_R^{(1)}} \ldots (X_R^{(n_R)} - \mu_{\iota(R,n_R)})^{i_R^{(n_R)}}]$$

where $m = i_S^{(1)} + i_I^{(1)} + \ldots + i_R^{(n_R)}$. Moments of order $m < 2$ are given by

$$\begin{aligned}
M_0 &= \mathbb{E}[1] = 1 \\
M_1 &= \mathbb{E}[(X_z^{(l)} - \mu_{\iota(z,l)})] = 0, \ \forall z \in \{S, I, R\}
\end{aligned}$$

Based on [26], $M_{i_S^{(1)},i_I^{(1)},i_R^{(1)},\ldots,i_R^{(n_R)}}$ of order $m \geq 2$ is given by

$$
\begin{aligned}
&\frac{dM_{i_S^{(1)},i_I^{(1)},i_R^{(1)},\ldots,i_R^{(n_R)}}}{dt} \\
&= \sum_{l=1}^{n_R}\Bigg[\lambda^{(l)}\mu_{\iota(S,l)}\mu_{\iota(I,l)} \sum_{h_S^{(l)}+h_I^{(l)}\neq i_S^{(l)}+i_I^{(l)}} \binom{i_S^{(l)}}{h_S^{(l)}}\binom{i_I^{(l)}}{h_I^{(l)}}(-1)^{i_S^{(l)}-h_S^{(l)}} M_{i_S^{(1)},\ldots,h_S^{(l)},h_I^{(l)},\ldots,i_R^{(n_R)}} \\
&+ \gamma\mu_{\iota(I,l)} \sum_{h_I^{(l)}+h_R^{(l)}\neq i_I^{(l)}+i_R^{(l)}} \binom{i_I^{(l)}}{h_I^{(l)}}\binom{i_R^{(l)}}{h_R^{(l)}}(-1)^{i_I^{(l)}-h_I^{(l)}} M_{i_S^{(1)},\ldots,h_I^{(l)},h_R^{(l)},\ldots,i_R^{(n_R)}} \\
&+ \alpha\mu_{\iota(R,l)} \sum_{h_S^{(l)}+h_R^{(l)}\neq i_S^{(l)}+i_R^{(l)}} \binom{i_S^{(l)}}{h_S^{(l)}}\binom{i_R^{(l)}}{h_R^{(l)}}(-1)^{i_R^{(l)}-h_R^{(l)}} M_{i_S^{(1)},\ldots,h_S^{(l)},i_I^{(l)},h_R^{(l)},\ldots,i_R^{(n_R)}} \\
&+ \sum_{k=l+1}^{n_R}\Bigg(\sum_{h_S^{(l)}+h_S^{(k)}\neq i_S^{(l)}+i_S^{(k)}} \binom{i_S^{(l)}}{h_S^{(l)}}\binom{i_S^{(k)}}{h_S^{(k)}} M_{i_S^{(1)},\ldots,h_S^{(l)},\ldots,h_S^{(k)},\ldots,i_R^{(n_R)}}\Big((-1)^{i_S^{(l)}-h_S^{(l)}}\kappa_S^{(l,k)}\mu_{\iota(S,l)} + (-1)^{i_S^{(k)}-h_S^{(k)}}\kappa_S^{(k,l)}\mu_{\iota(S,k)}\Big) \\
&+ \sum_{h_I^{(l)}+h_I^{(k)}\neq i_I^{(l)}+i_I^{(k)}} \binom{i_I^{(l)}}{h_I^{(l)}}\binom{i_I^{(k)}}{h_I^{(k)}} M_{i_S^{(1)},\ldots,h_I^{(l)},\ldots,h_I^{(k)},\ldots,i_R^{(n_R)}}\Big((-1)^{i_I^{(l)}-h_I^{(l)}}\kappa_I^{(l,k)}\mu_{\iota(I,l)} + (-1)^{i_I^{(k)}-h_I^{(k)}}\kappa_I^{(k,l)}\mu_{\iota(I,k)}\Big) \\
&+ \sum_{h_R^{(l)}+h_R^{(k)}\neq i_R^{(l)}+i_R^{(k)}} \binom{i_R^{(l)}}{h_R^{(l)}}\binom{i_R^{(k)}}{h_R^{(k)}} M_{i_S^{(1)},\ldots,h_R^{(l)},\ldots,h_R^{(k)},\ldots,i_R^{(n_R)}}\Big((-1)^{i_R^{(l)}-h_R^{(l)}}\kappa_R^{(l,k)}\mu_{\iota(R,l)} + (-1)^{i_R^{(k)}-h_R^{(k)}}\kappa_R^{(k,l)}\mu_{\iota(R,k)}\Big)\Bigg) \\
&+ \sum_{h_S^{(l)}+h_I^{(l)}\neq i_S^{(l)}+i_I^{(l)}} \binom{i_S^{(l)}}{h_S^{(l)}}\binom{i_I^{(l)}}{h_I^{(l)}}(-1)^{i_S^{(l)}-h_S^{(l)}} \cdot \Big(\Big(\lambda^{(l)}\mu_{\iota(I,l)} M_{i_S^{(1)},\ldots,h_S^{(l)}+1,h_I^{(l)},\ldots,i_R^{(n_R)}} \\
&+ \lambda^{(l)}\mu_{\iota(S,l)} M_{i_S^{(1)},\ldots,h_S^{(l)},h_I^{(l)}+1,\ldots,i_R^{(n_R)}}\Big)\Big) + \gamma \sum_{h_I^{(l)}+h_R^{(l)}\neq i_I^{(l)}+i_R^{(l)}} \binom{i_I^{(l)}}{h_I^{(l)}}\binom{i_R^{(l)}}{h_R^{(l)}}(-1)^{i_I^{(l)}-h_I^{(l)}} M_{i_S^{(1)},\ldots,h_I^{(l)}+1,h_R^{(l)},\ldots,i_R^{(n_R)}} \\
&+ \alpha \sum_{h_S^{(l)}+h_R^{(l)}\neq i_S^{(l)}+i_R^{(l)}} \binom{i_S^{(l)}}{h_S^{(l)}}\binom{i_R^{(l)}}{h_R^{(l)}}(-1)^{i_R^{(l)}-h_R^{(l)}} M_{i_S^{(1)},\ldots,h_S^{(l)},i_I^{(l)},h_R^{(l)}+1,\ldots,i_R^{(n_R)}} \\
&+ \sum_{k=l+1}^{n_R}\Bigg(\sum_{h_S^{(l)}+h_S^{(k)}\neq i_S^{(l)}+i_S^{(k)}} \binom{i_S^{(l)}}{h_S^{(l)}}\binom{i_S^{(k)}}{h_S^{(k)}}\Big((-1)^{i_S^{(l)}-h_S^{(l)}}\kappa_S^{(l,k)} M_{i_S^{(1)},\ldots,h_S^{(l)}+1,\ldots,h_S^{(k)},\ldots,i_R^{(n_R)}} \\
&+ (-1)^{i_S^{(k)}-h_S^{(k)}}\kappa_S^{(k,l)} M_{i_S^{(1)},\ldots,h_S^{(l)},\ldots,h_S^{(k)}+1,\ldots,i_R^{(n_R)}}\Big) \\
&+ \sum_{h_I^{(l)}+h_I^{(k)}\neq i_I^{(l)}+i_I^{(k)}} \binom{i_I^{(l)}}{h_I^{(l)}}\binom{i_I^{(k)}}{h_I^{(k)}}\Big((-1)^{i_I^{(l)}-h_I^{(l)}}\kappa_I^{(l,k)} M_{i_S^{(1)},\ldots,h_I^{(l)}+1,\ldots,h_I^{(k)},\ldots,i_R^{(n_R)}} \\
&+ (-1)^{i_I^{(k)}-h_I^{(k)}}\kappa_I^{(k,l)} M_{i_S^{(1)},\ldots,h_I^{(l)},\ldots,h_I^{(k)}+1,\ldots,i_R^{(n_R)}}\Big) + \sum_{h_R^{(l)}+h_R^{(k)}\neq i_R^{(l)}+i_R^{(k)}} \binom{i_R^{(l)}}{h_R^{(l)}}\binom{i_R^{(k)}}{h_R^{(k)}} \\
&\Big((-1)^{i_R^{(l)}-h_R^{(l)}}\kappa_R^{(l,k)} M_{i_S^{(1)},\ldots,h_R^{(l)}+1,\ldots,h_R^{(k)},\ldots,i_R^{(n_R)}} + (-1)^{i_R^{(k)}-h_R^{(k)}}\kappa_R^{(k,l)} M_{i_S^{(1)},\ldots,h_R^{(l)},\ldots,h_R^{(k)}+1,\ldots,i_R^{(n_R)}}\Big)\Big) \\
&+ \lambda^{(l)} \sum_{h_S^{(l)}+h_I^{(l)}\neq i_S^{(l)}+i_I^{(l)}} \binom{i_S^{(l)}}{h_S^{(l)}}\binom{i_I^{(l)}}{h_I^{(l)}}(-1)^{i_S^{(l)}-h_S^{(l)}} M_{i_S^{(1)},\ldots,h_S^{(l)}+1,h_I^{(l)}+1,\ldots,i_R^{(n_R)}} \\
&- i_S^{(l)}\mu'_{\iota(S,l)} M_{i_S^{(1)},\ldots,i_S^{(l)}-1,\ldots,i_R^{(n_R)}} - i_I^{(l)}\mu'_{\iota(I,l)} M_{i_S^{(1)},\ldots,i_I^{(l)}-1,\ldots,i_R^{(n_R)}} - i_R^{(l)}\mu'_{\iota(R,l)} M_{i_S^{(1)},\ldots,i_R^{(l)}-1,\ldots,i_R^{(n_R)}}\Bigg]
\end{aligned}
\tag{A.1}
$$

Appendix B. Supplementary Algorithms

Algorithm 1: Temporal-spatial hybrid simulation

Initialize stochastic model for all regions, moment equations with zeros, Δt with $\Delta t_{sw} = \Delta t_{ex}$ and t with t_0
While $t < t_{\max}$

Foreach stochastically modeled region k
If $\Gamma^{(S \to D)}(\mathbf{X}) = 1$
Forall infection states $z \in \{S, I, R\}$
$\mu^D_{\iota(z,k)}(t) = \mu^S_{\iota(z,k)}(t)$
Forall infection states $y \in \{S, I, R\}$
$\sigma^D_{\iota(y,k),\iota(z,k)}(t) = \sigma^S_{\iota(y,k),\iota(z,k)}(t)$
Forall $s = 1, \ldots, n_{sims}$
$X^{(k)}_{z,s} = 0$
Set infection state transition and outgoing spatial transition rates
for region k in moment equation-based model
Remove infection state transition and outgoing spatial transition rates
for region k in stochastic model

Convert stochastic to MoM

Foreach region l modeled with moment equations
If $\Gamma^{(D \to S)}\left(\left[\mu^D(t), \Sigma^D(t)\right]^\top\right) = 1$
Forall infection states $z \in \{S, I, R\}$
$\xi_{\iota(z,l)} = 0$
Forall $s = 1, ..., n_{sims}$
$\tilde{X}^{(l)}_{z,s} \sim \mathcal{N}(\mu^D_{\iota(z,l)}, \sigma^D_{\iota(z,l),\iota(z,l)})$
$X^{(l)}_{z,s} = \max\{0, \lfloor \tilde{X}^{(l)}_{z,s} + \xi_{\iota(z,l)} \rceil\}$
$\xi_{\iota(z,l)} = \tilde{X}^{(l)}_{z,s} + \xi_{\iota(z,l)} - X^{(l)}_{z,s}$
$\mu^D_{\iota(z,l)}(t) = 0$
Forall infection states $y \in \{S, I, R\}$
$\sigma^D_{\iota(y,l),\iota(z,l)}(t) = 0$
Set infection state transition and outgoing spatial transition rates
for region l in stochastic model
Remove infection state transition and outgoing spatial transition rates
for region l in moment equation-based model

Convert MoM to stochastic model

$t = \min\{t_{max}, t + \Delta t\}$
Advance both models until t

Foreach stochastically modeled region k
Forall infection states $z \in \{S, I, R\}$
If $\mu^D_{\iota(z,k)}(t) > 0$
$\xi_{\iota(z,k)} = 0$
Forall $s = 1, \ldots, n_{sims}$
$\tilde{X}^{(k)}_{z,s} \sim \mathcal{N}(\mu^D_{\iota(z,k)}, \sigma^D_{\iota(z,k),\iota(z,k)})$
$\Delta X^{(k)}_{z,s} = \max\{0, \lfloor \tilde{X}^{(k)}_{z,s} + \xi_{\iota(z,k)} \rceil\}$
$X^{(k)}_{z,s} += \Delta X^{(k)}_{z,s}$
$\xi_{\iota(z,k)} = \tilde{X}^{(k)}_{z,s} + \xi_{\iota(z,k)} - \Delta X^{(k)}_{z,s}$
$\mu^D_{\iota(z,k)}(t) = 0$
Forall infection states $y \in \{S, I, R\}$
$\sigma^D_{\iota(y,k),\iota(z,k)}(t) = 0$

Exchange subpopulations from moment equations to stochastic model

Foreach region l modeled with moment equations
Foreach infection state $z \in \{S, I, R\}$
If $\mu^S_{\iota(z,l)}(t) > 0$
$\mu^D_{\iota(z,l)}(t) += \mu^S_{\iota(z,l)}(t)$
$\sigma^D_{\iota(z,l),\iota(z,l)} \sim U\left(\left(\sqrt{\sigma^D_{\iota(z,l),\iota(z,l)}} - \sqrt{\sigma^S_{\iota(z,l),\iota(z,l)}}\right)^2, \left(\sqrt{\sigma^D_{\iota(z,l),\iota(z,l)}} + \sqrt{\sigma^S_{\iota(z,l),\iota(z,l)}}\right)^2\right)$
Forall $s = 1, ..., n_{sims}$
$X^{(l)}_{z,s} = 0$

Exchange subpopulations from stochastic model to moment equations

Appendix C. Supplementary Figures

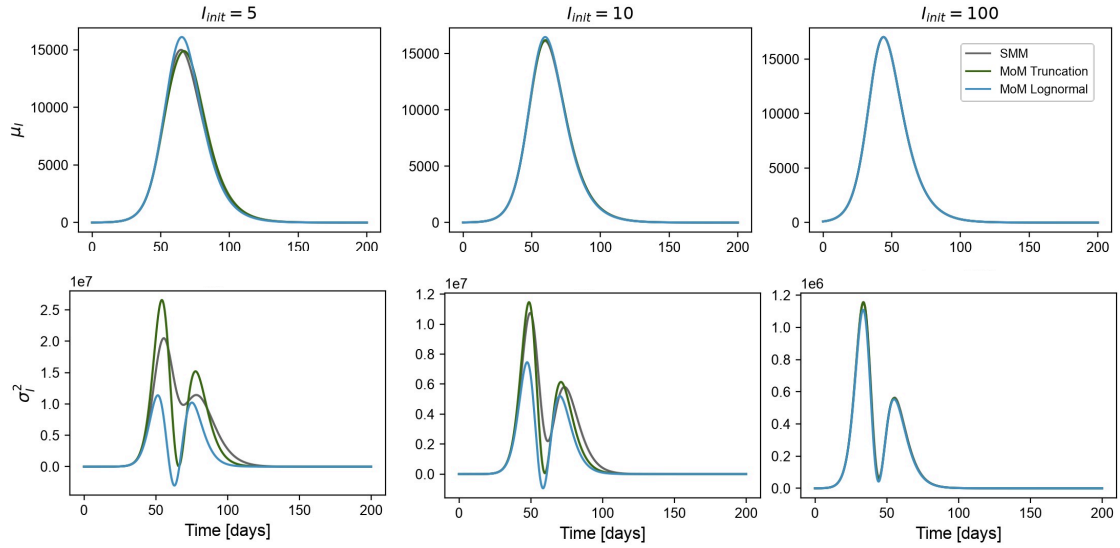


Figure C.10: Comparison of truncation closure and lognormal distributional closure. Both closure methods approximate the mean (top) and the variance (bottom) differently well for varying initial conditions. The ground truth values (SMM) are obtained from 10,000 Gillespie simulations of the stochastic model.

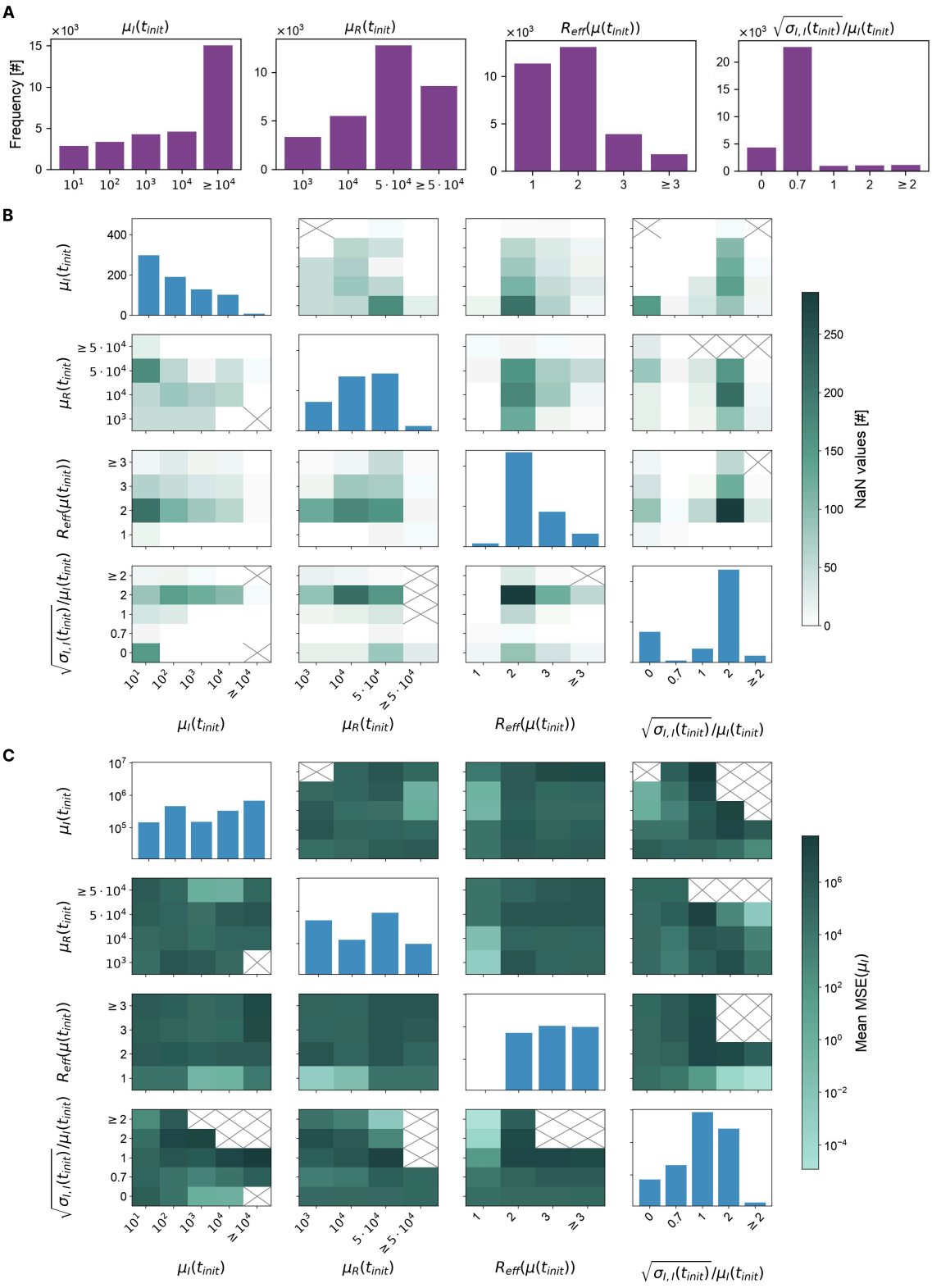


Figure C.11: Performance analysis of the MoM for the SIRS model. For the analysis 50, 000 stochastic runs were compared to the solution of the moment equations using truncation closure for each parameter set. **A:** Distribution of initial conditions. **B:** Distribution of NaN value counts. **C:** Mean MSE of the simulated mean number of infected μ_I.

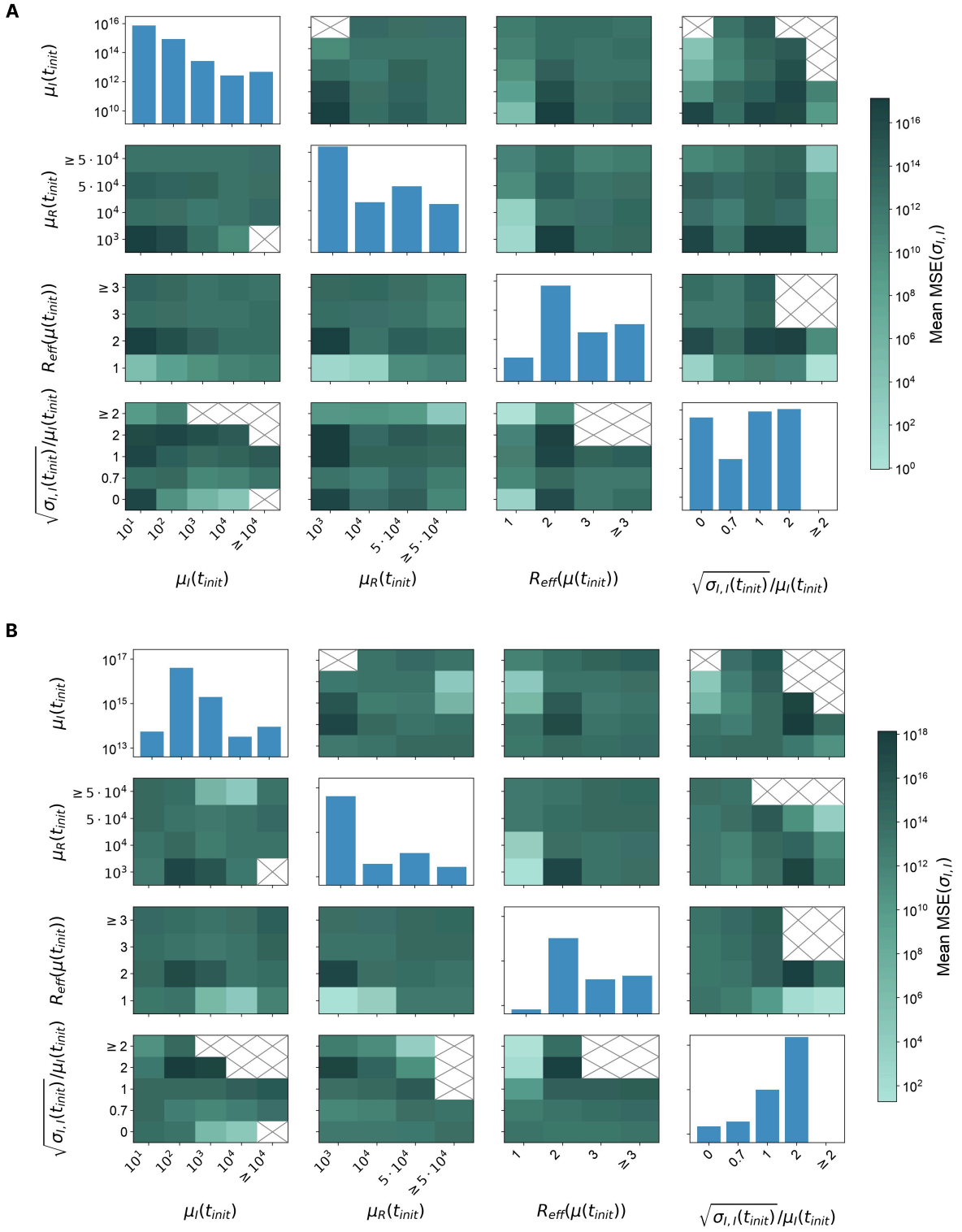


Figure C.12: Performance analysis of the MoM for the variance of the SIR and SIRS model. Mean MSE of the simulated variance of the infected compartment σ_I for **A:** the SIR model and **B:** the SIRS model.

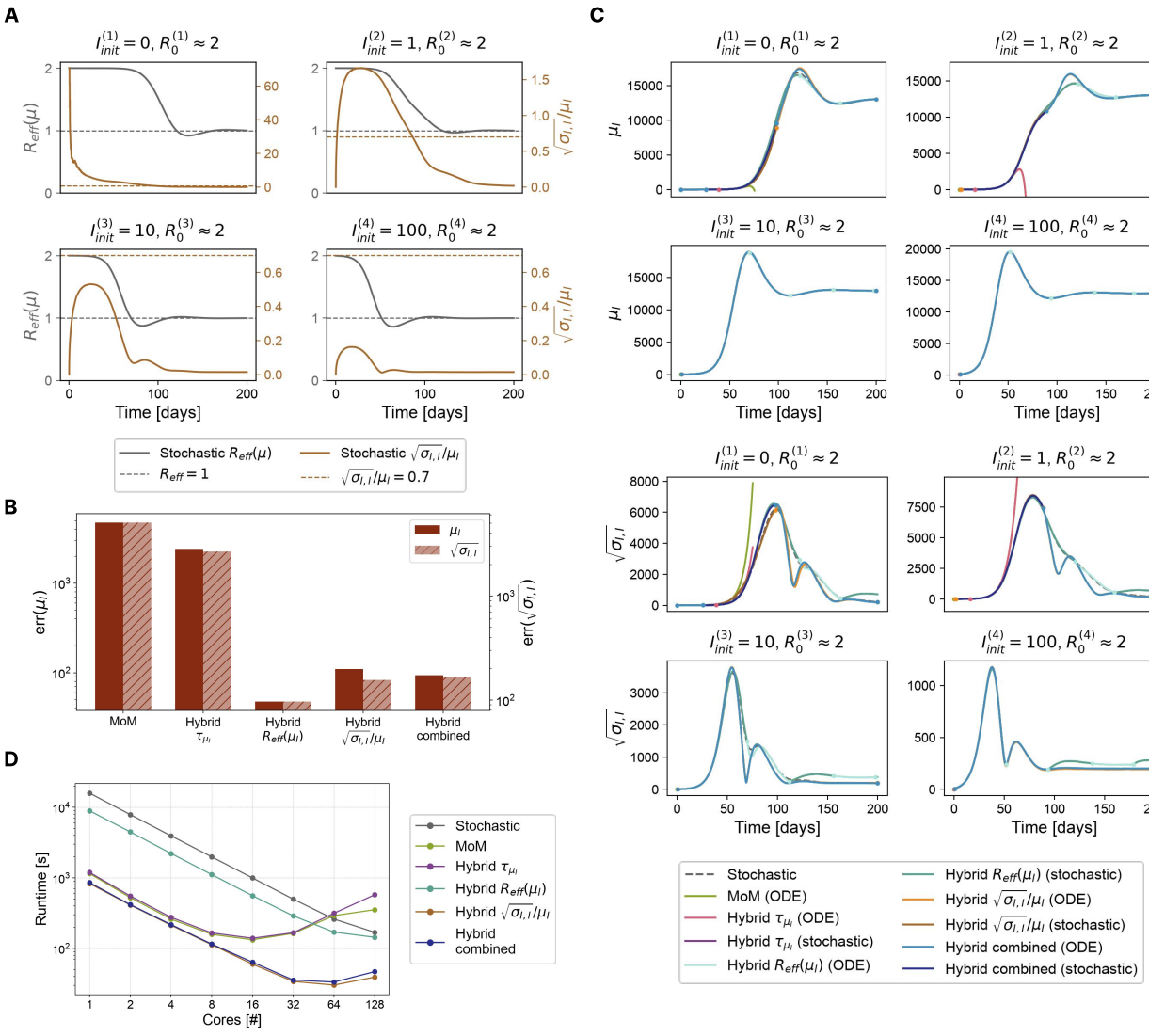


Figure C.13: Results of different condition functions for the SIRS-type model with four regions and a varying number of initially infected per region. Shown are the results of 10,000 simulations for each model. **A:** Temporal evolution of the relative standard deviation of the I compartment and the reproduction number of the mean for each region. The horizontal dashed lines indicate the threshold values used for the corresponding conditions. **B:** Mean absolute error in mean and standard deviation of the moment-closure approximation and the hybrid model with four different conditions. **C:** Evolution of mean (top) and standard deviation (bottom) in every region for the stochastic model, the moment-closure approximation and the hybrid model with four different conditions. For the hybrid model the stochastic parts are displayed in a dark and the deterministic parts in a light color shade. **D:** Strong scaling of the stochastic model (Stochastic), the moment-closure approximation (MoM), and the hybrid models using the absolute threshold condition (τ_{μ_I}), the reproduction number condition ($R_{eff}(\mu_I)$), the standard deviation relation condition ($\frac{\sqrt{\sigma_{I,I}}}{\mu_I}$) and the combined condition.

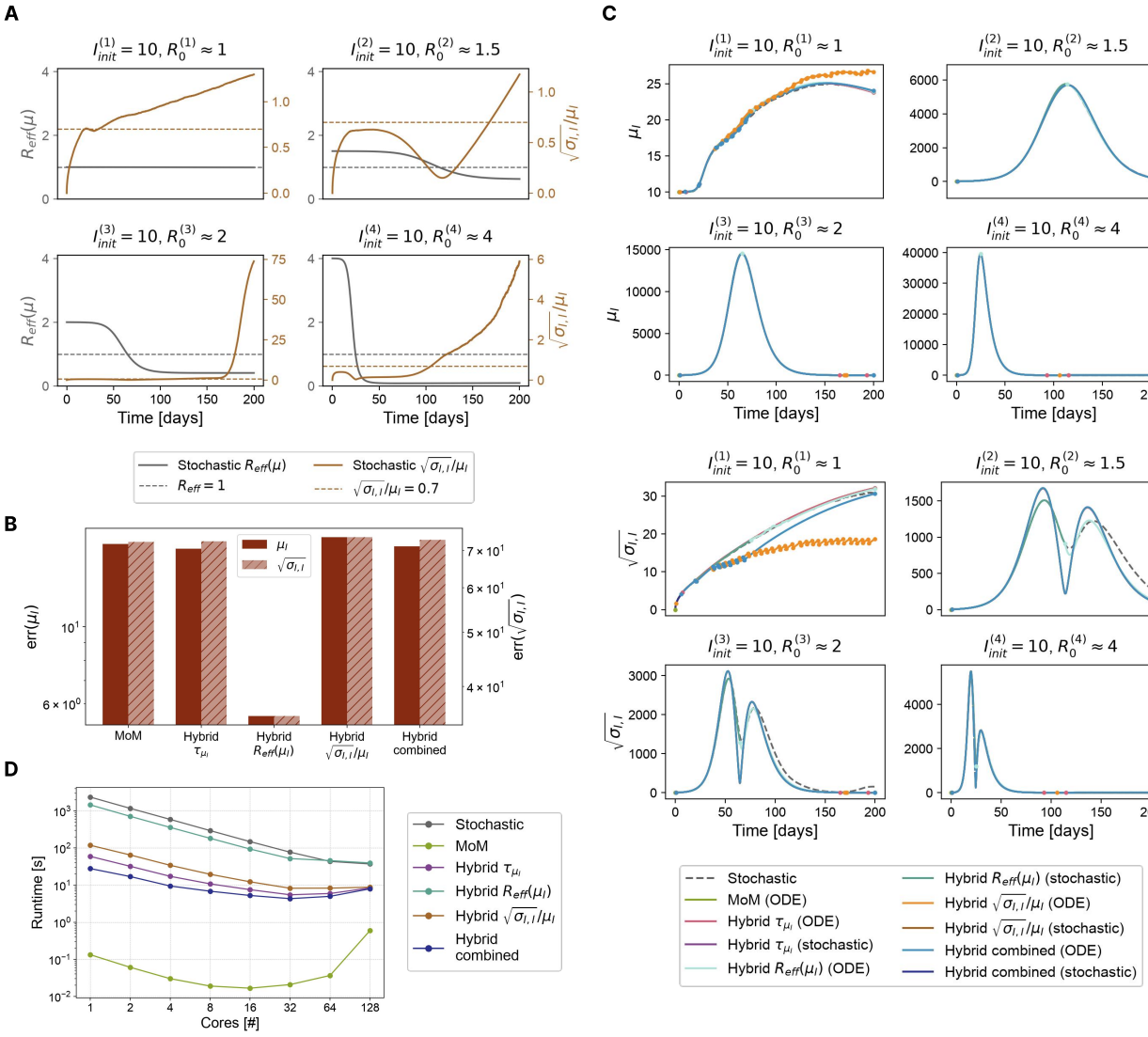


Figure C.14: Results of different condition functions for the SIR-type model with four regions and region-dependent transmission rates. Shown are the results of 10,000 simulations for each model. **A:** Temporal evolution of the relative standard deviation of the I compartment and the reproduction number of the mean for each region. The horizontal red lines indicate the threshold values used for the corresponding conditions. **B:** Mean absolute error in mean and standard deviation of the moment-closure approximation and the hybrid model with four different conditions. **C:** Evolution of mean (top) and standard deviation (bottom) in every region for the stochastic model, the moment-closure approximation and the hybrid model with four different conditions. For the hybrid model the stochastic parts are displayed in a dark and the deterministic parts in a light color shade. **D:** Strong scaling of the stochastic model (Stochastic), the moment-closure approximation (MoM), and the hybrid models using the absolute threshold condition (τ_{μ_I}), the reproduction number condition ($R_{eff}(\mu_I)$), the standard deviation relation condition ($\frac{\sqrt{\sigma_{I,I}}}{\mu_I}$) and the combined condition.

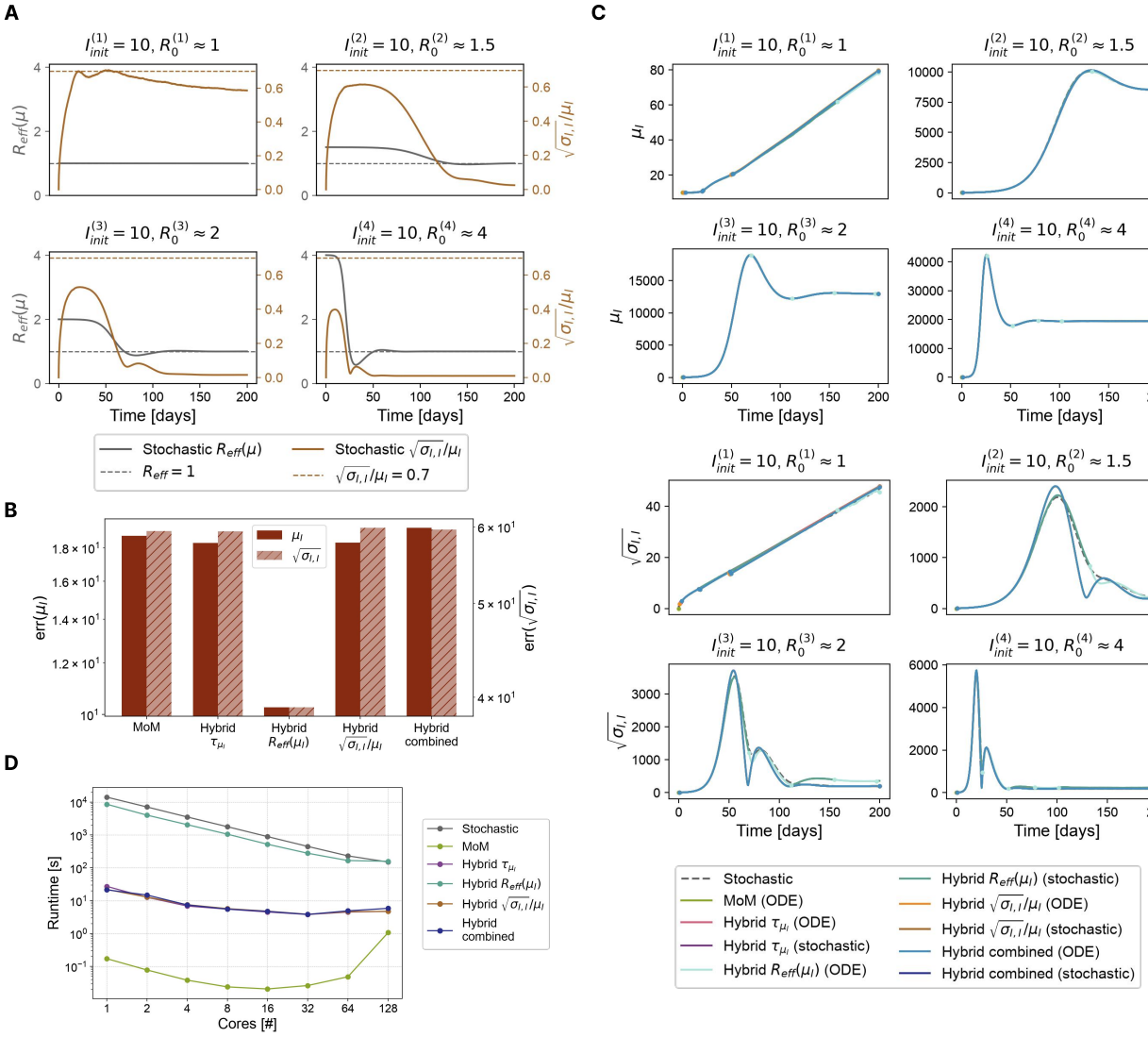


Figure C.15: Results of different condition functions for the SIRS-type model with four regions and region-dependent transmission rates. Shown are the results of 10,000 simulations for each model. **A:** Temporal evolution of the relative standard deviation of the I compartment and the reproduction number of the mean for each region. The horizontal red lines indicate the threshold values used for the corresponding conditions. **B:** Mean absolute error in mean and standard deviation of the moment-closure approximation and the hybrid model with four different conditions. **C:** Evolution of mean (top) and standard deviation (bottom) in every region for the stochastic model, the moment-closure approximation and the hybrid model with four different conditions. For the hybrid model the stochastic parts are displayed in a dark and the deterministic parts in a light color shade. **D:** Strong scaling of the stochastic model (Stochastic), the moment-closure approximation (MoM), and the hybrid models using the absolute threshold condition (τ_{μ_I}), the reproduction number condition ($R_{eff}(\mu_I)$), the standard deviation relation condition ($\frac{\sqrt{\sigma_{I,I}}}{\mu_I}$) and the combined condition.

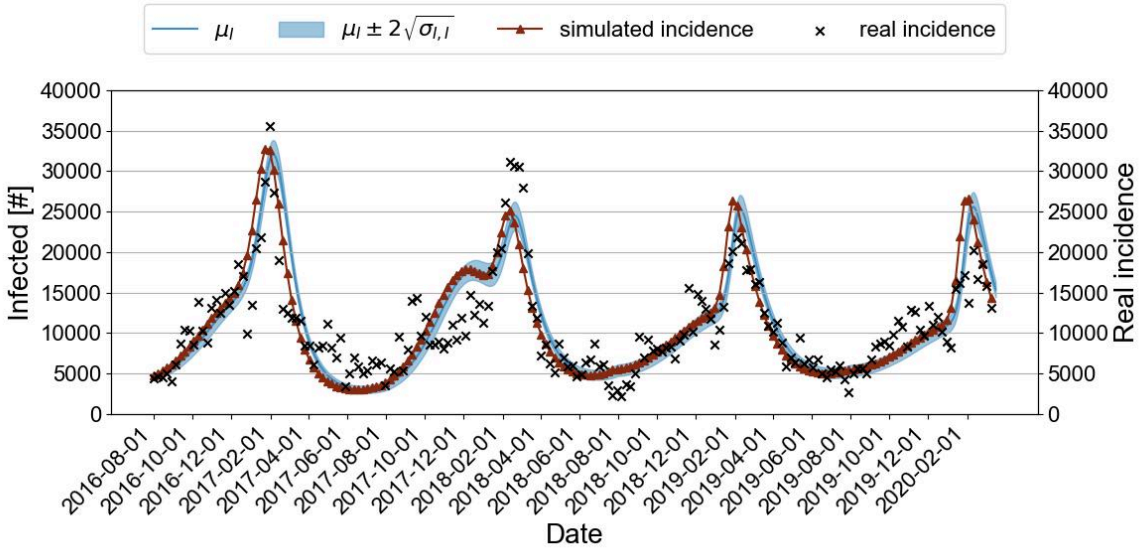


Figure C.16: Simulated influenza infected from 1st August 2016 to 9th March 2020 compared to scaled reported incidence.

Appendix D. Supplementary Tables

Parameter	Description	Value per scenario		
		Setting 1	Setting 2	Setting 3
N	Total population size	Ranging from $10^3 - 10^7$	10^6 equally distributed across regions	10^6 equally distributed across regions
n_R	Number of regions	1	Ranging from $2^0 - 2^4$	Ranging from $2^0 - 2^4$
$\mu_{\iota(I,k)}(t_0)$	Mean number of initially infected per region	10	10	10
$\mu_{\iota(R,k)}(t_0)$	Mean number of initially recovered per region	0	0	0
γ	Recovery rate in days^{-1}	$\frac{1}{7}$	$\frac{1}{7}$	$\frac{1}{7}$
α	Immunity waning rate in days^{-1}	0 (SIR), $\frac{1}{20}$ (SIRS)	0 (SIR), $\frac{1}{20}$ (SIRS)	0 (SIR), $\frac{1}{20}$ (SIRS)
$\lambda^{(k)}$	Transmission rate per region	$\frac{2.5\gamma}{N^{(k)}}$	$\frac{2.5\gamma}{N^{(k)}}$	$\frac{2.5\gamma}{N^{(k)}}$
$\kappa_z^{(k,l)}$	Spatial transition rate	0	0	10^{-4}

Table D.1: Parameters used for scaling simulation study.

Parameter	Description	Value	Reference
Δt_{max}	Time interval in days at which model outcomes are saved	0.1	
n_R	Number of modeled regions	1 (global); 4 (regional)	[53]
n_{sims}	Number of simulations used for the stochastic model	5,000	
$\mu_{\iota(I,k)}(t_0)$	Mean number of initially infected per region	4,407 (global); 320 (North), 1,000 (East), 1,400 (South), 1,000 (West)	calibrated
$\mu_{\iota(R,k)}(t_0)$	Mean number of initially recovered per region	198,228 (global); 50,000 (North), 40,220 (East), 41,850 (South), 37,700 (West)	calibrated
$N^{(k)}$	Initial population size per region	835,771 (global); 135,314 (North), 160,939 (East), 244,948 (South), 294,569 (West)	[62], accessed via [63]
γ	Recovery rate in days^{-1}	$1/7$	[51, 52]
α	Waning immunity rate in days^{-1}	$1/149$	calibrated
λ_0	Peak transmission rate	$2.9086e-7$ (global); $1.7992e-6$ (North), $1.5318e-6$ (East), $9.7867e-7$ (South), $8.1521e-7$ (West)	calibrated
$t^{(peak)}$	Transmission rate peak time point per season in days	$(174, 555, 907, 1272, 1637)$	calibrated
ρ	Minimal transmission rate proportion per season	$(0.81, 0.83, 0.8, 0.78, 0.805)$	calibrated
σ	Seasonality standard deviation	$(20, 15, 10, 10, 12.5)$	calibrated
$d^{(1)} = (d^{(1)}_{North}, d^{(1)}_{East}, d^{(1)}_{South}, d^{(1)}_{West})$	First damping factor applied at 16th March 2020	$(1,1,1,1)$ (Base), $(0.4, 0.4, 0.4, 0.4)$ (Global NPIs, Global NPIs total lifting), $(0.4, 0.4, 0.3, 0.4)$ (Stricter NPIs in the South), $(0.4, 0.4, 1, 0.4)$ (No NPIs in the South)	[55]
$d^{(2)} = (d^{(2)}_{North}, d^{(2)}_{East}, d^{(2)}_{South}, d^{(2)}_{West})$	Second damping factor applied at 15th April 2020	$(1,1,1,1)$ (Base), $(\frac{0.95}{0.4}, \frac{0.95}{0.4}, \frac{0.95}{0.4}, \frac{0.95}{0.4})$ (Global NPIs, Global NPIs total lifting), $(\frac{0.95}{0.4}, \frac{0.95}{0.4}, \frac{0.95}{0.3}, \frac{0.95}{0.4})$ (Stricter NPIs in the South), $(\frac{0.95}{0.4}, \frac{0.95}{0.4}, 1, \frac{0.95}{0.4})$ (No NPIs in the South)	[55]
$d^{(3)} = (d^{(3)}_{North}, d^{(3)}_{East}, d^{(3)}_{South}, d^{(3)}_{West})$	Third damping factor applied at 2nd November 2020	$(1,1,1,1)$ (Base), $(\frac{0.8}{0.95}, \frac{0.8}{0.95}, \frac{0.8}{0.95}, \frac{0.8}{0.95})$ (Global NPIs, Global NPIs total lifting), $(\frac{0.8}{0.95}, \frac{0.8}{0.95}, \frac{0.7}{0.95}, \frac{0.8}{0.95})$ (Stricter NPIs in the South), $(\frac{0.8}{0.95}, \frac{0.8}{0.95}, 1, \frac{0.8}{0.95})$ (No NPIs in the South)	[55]
$d^{(4)} = (d^{(4)}_{North}, d^{(4)}_{East}, d^{(4)}_{South}, d^{(4)}_{West})$	Fourth damping factor applied at 25th November 2020	$(1,1,1,1)$ (Base), $(\frac{0.7}{0.8}, \frac{0.7}{0.8}, \frac{0.7}{0.8}, \frac{0.7}{0.8})$ (Global NPIs, Global NPIs total lifting), $(\frac{0.7}{0.8}, \frac{0.7}{0.8}, \frac{0.6}{0.7}, \frac{0.7}{0.8})$ (Stricter NPIs in the South), $(\frac{0.7}{0.8}, \frac{0.7}{0.8}, 1, \frac{0.7}{0.8})$ (No NPIs in the South)	[55]
$d^{(5)} = (d^{(5)}_{North}, d^{(5)}_{East}, d^{(5)}_{South}, d^{(5)}_{West})$	Fifth damping factor applied at 8th March 2021	$(1,1,1,1)$ (Base), $(\frac{0.85}{0.7}, \frac{0.85}{0.7}, \frac{0.85}{0.7}, \frac{0.85}{0.7})$ (Global NPIs, Global NPIs total lifting), $(\frac{0.85}{0.7}, \frac{0.85}{0.7}, \frac{0.85}{0.6}, \frac{0.85}{0.7})$ (Stricter NPIs in the South), $(\frac{0.85}{0.7}, \frac{0.85}{0.7}, 1, \frac{0.85}{0.7})$ (No NPIs in the South)	[55]
$d^{(6)} = (d^{(6)}_{North}, d^{(6)}_{East}, d^{(6)}_{South}, d^{(6)}_{West})$	Sixth damping factor applied at 3rd May 2021	$(1,1,1,1)$ (Base), $(1,1,1,1)$ (Global NPIs), $(\frac{1}{0.85}, \frac{1}{0.85}, \frac{1}{0.85}, \frac{1}{0.85})$ (Global NPIs total lifting), $(1,1,1,1)$ (Stricter NPIs in the South), $(1,1,1,1)$ (No NPIs in the South)	[55]

Table D.2: Parameters used for the (regional) influenza application.